nature cell biology

Functional differentiation of cooperating kinesin-2 motors orchestrates cargo import and transport in *C. elegans* cilia

Bram Prevo[1], Pierre Mangeol[1,3,4], Felix Oswald[1,4], Jonathan M. Scholey[2] and Erwin J. G. Peterman[1,5]

Intracellular transport depends on cooperation between distinct motor proteins. Two anterograde intraflagellar transport (IFT) motors, heterotrimeric kinesin-II and homodimeric OSM-3, cooperate to move cargo along *Caenorhabditis elegans* cilia. Here, using quantitative fluorescence microscopy, with single-molecule sensitivity, of IFT in living strains containing single-copy transgenes encoding fluorescent IFT proteins, we show that kinesin-II transports IFT trains through the ciliary base and transition zone to a 'handover zone' on the proximal axoneme. There, OSM-3 gradually replaces kinesin-II, yielding velocity profiles inconsistent with *in vitro* motility assays, and then drives transport to the ciliary tip. Dissociated kinesin-II motors undergo rapid turnaround and recycling to the ciliary base, whereas OSM-3 is recycled mainly to the handover zone. This reveals a functional differentiation in which the slower, less processive kinesin-II imports IFT trains into the cilium and OSM-3 drives their long-range transport, thereby optimizing cargo delivery.

Intracellular transport systems that use microtubule-based motor proteins play critical roles in eukaryotic cells[1–5]. These systems often depend on the functional cooperation between different types of microtubule-based motor[6], for example between opposite-polarity kinesin and dynein motors that generate bidirectional axonal or intraflagellar transport (IFT) within neurons and cilia, respectively[1,4,7,8]. Some forms of transport, however, use cooperating same-polarity microtubule motors. For example, within chemosensory cilia of *Caenorhabditis elegans*, two types of plus-end-directed kinesin-2 motor cooperate to drive anterograde IFT (ref. 9). How and why teams of distinct, same-polarity motors transport the same cargo is unclear[8,10–14].

Cilia, which participate in both motility and signalling, consist of a membrane-bounded axoneme constructed from 9 doublet microtubules projecting from the cell surface with their plus ends distal[15]. Cilium biogenesis requires kinesin-2-driven anterograde IFT (ref. 16) of IFT trains (ref. 17) assembled from multiple ~17S IFT particles (comprising multi-protein subcomplexes IFT-A and IFT-B; ref. 18), which cross the 'periciliary barrier'[19,20] and then deliver ciliary precursors to the distal tip[21–24]. In *Chlamydomonas*, one motor, heterotrimeric kinesin-2 (refs 3,25), drives anterograde IFT (refs 18,26,27), whereas IFT dynein mediates retrograde transport[28,29]. Retrograde transport in *C. elegans* amphid or phasmid cilia is also mediated by IFT dynein[30], but anterograde IFT depends on the collaboration between two types of kinesin-2, heterotrimeric kinesin-II and homodimeric OSM-3 (refs 3,9,10,31).

The axonemes of *C. elegans* cilia emanate from the ciliary base and transition zone (TZ), and have a bipartite structure consisting of the proximal (also known as middle) segment (PS) made of 9 doublet microtubules from which 9 singlet microtubules extend to form the distal segment[32,33] (DS; Fig. 1a). Kinesin-II and OSM-3 together transport IFT trains along the PS to deliver axoneme subunits for PS assembly, whereas DS assembly depends on the transport of precursors driven by OSM-3 alone[9,32,34]. *In vitro*, kinesin-II generates short, slow runs (~0.2 μm at ~0.5 μm s^{-1}), and OSM-3 generates longer, faster runs (~2 μm at ~1.5 μm s^{-1}; refs 10,35,36), but the advantage of using both motors to move the same cargo along the PS at the intermediate speed of ~0.7 μm s^{-1} is unclear. Understanding this may illuminate how distinct same-polarity motors cooperate generally and may reveal the functions of different kinesin-2 motors in a broad range of cilia[37,38].

Here we investigate why employing these two distinct forms of kinesin-2 may be functionally advantageous. We improved on previous work by replacing endogenous IFT proteins with native levels

[1]Department of Physics and Astronomy and LaserLaB Amsterdam, VU University Amsterdam, De Boelelaan 1081, 1081 HV Amsterdam, The Netherlands. [2]Department of Molecular and Cellular Biology, University of California at Davis, Davis, California 95616, USA. [3]Present address: Biology Institute of Marseille, Aix-Marseille University, 13288 Marseille Cedex 9, France. [4]These authors contributed equally to this work.
[5]Correspondence should be addressed to E.J.G.P. (e-mail: e.j.g.peterman@vu.nl)

Received 3 June 2015; accepted 30 September 2015; published online 2 November 2015; DOI: 10.1038/ncb3263

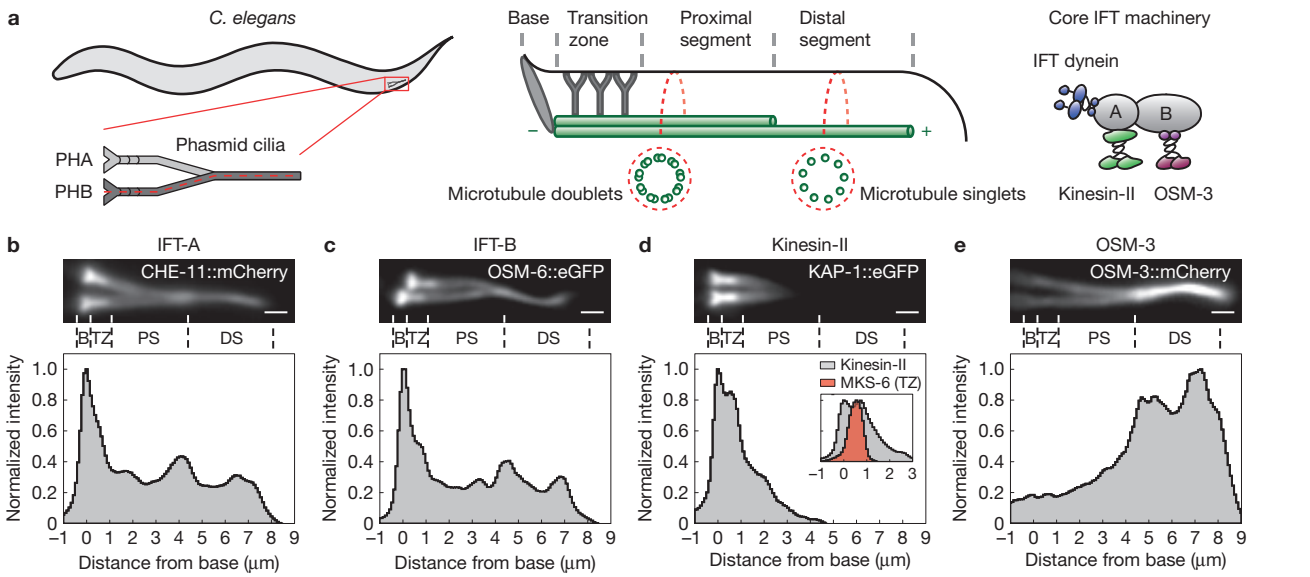

Figure 1 IFT-particle subcomplexes and IFT motors show distinct localization patterns along cilia. (**a**) Schematic diagrams depicting *C. elegans* and the location of the phasmid cilia, their structure and cross-sections showing microtubules (green, minus (−) and plus (+) denote microtubule polarity), and the core IFT machinery. (**b**–**e**) Representative time-averaged fluorescence images (top) and corresponding fluorescence-intensity profiles (bottom) along the lower cilium (corresponding to the red dashed line in **a** left). Scale bars, 1 μm. B, base; TZ, transition zone; PS, proximal segment; DS, distal segment. All fluorescence-intensity profiles are normalized to their maximum. (**b**) IFT-A (CHE-11::mCherry, an IFT-particle-subcomplex A subunit); (**c**) IFT-B (OSM-6::eGFP, an IFT-particle-subcomplex B subunit); (**d**) Kinesin-II (KAP-1::eGFP, a non-motor accessory subunit of heterotrimeric kinesin-2 complexes[58]); (**e**) OSM-3 (OSM-3::mCherry). The inset in **d** is an overlay of the kinesin-II distribution with that of a transition zone marker (MKS-6::mCherry; Supplementary Fig. 1a, from 20 worms). For number of worms imaged to obtain representative images, see Supplementary Fig. 6a-d.

of functional, fluorescent IFT proteins using single genome-integrated transgenes containing natural regulatory sequences, combined with ultrasensitive, laser-illuminated epi-fluorescence microscopy. This allowed quantitative dissection of the IFT system at the single-protein, IFT-train and cilium levels within living *C. elegans*, at unprecedented resolution and with minimal perturbation of IFT dynamics.

RESULTS

IFT proteins exhibit unexpected differences in their distribution

We first examined the distribution of mCherry or eGFP-tagged IFT motors, kinesin-II and OSM-3 and IFT-particle subcomplexes, IFT-A and IFT-B, relative to the structurally dense TZ, which serves as a periciliary barrier (Fig. 1a; for strains, see Supplementary Table 1). We observed that IFT-A and IFT-B were distributed along the cilium with a peak at the base, a shoulder extending into the TZ and a small bump at the PS-to-DS transition, consistent with previous studies[9,23,31,34] (Fig. 1b,c). Surprisingly, however, the distribution of the kinesin-2 motors was different from those reported previously[9,23,31,34]. Instead of being evenly distributed along the PS, kinesin-II was highly enriched at the base and TZ (Fig. 1d and Supplementary Fig. 1a,b and Table 1) whereas OSM-3 mainly localized at the DS instead of distributing evenly along the entire axoneme (Fig. 1e and Supplementary Fig. 1c and Table 1). Strikingly, relatively little of either motor was observed along the PS. To understand these localization patterns, we studied the dynamics of the IFT-particle subcomplexes and kinesin-2 motors.

Dynamics of IFT trains

Sequential images of IFT-particle subcomplexes and motors (Supplementary Videos 1 and 2) were analysed using kymography with Fourier filtering to quantify the composition and motility of IFT components (Fig. 2a). Anterograde IFT trains exhibited surprisingly rich dynamics, assembling at the ciliary base, entering in bursts, similar to IFT-train entry in *Chlamydomonas*[39], and then gradually accelerating through the TZ and along the PS, before reaching their maximal velocity along the DS (Fig. 2b and Supplementary Fig. 2a). At about 2–3 μm from the base, IFT trains often splay apart into discrete particles moving at slightly different velocities (Fig. 2b and Supplementary Fig. 2a). This could represent several discrete IFT trains that enter the cilium together and then separate or a single IFT train that depolymerizes into smaller trains. In contrast, retrograde IFT trains move at relatively constant velocity from ciliary tip to TZ, where they decelerate (Supplementary Fig. 2b,c). On the basis of IFT-train intensity, retrograde trains contain fewer IFT-particle subcomplexes than anterograde trains (Supplementary Fig. 2a,b,d), consistent with electron microscopy data in *Chlamydomonas*[17]. Except at the base where train formation occurs, and around the TZ where trains splay apart, the intensity of IFT-particle subcomplexes stays constant, indicating that IFT-particle subcomplexes polymerize to form stable IFT-train backbones that remain intact during long-range transport along the cilium.

Motor cooperation defines regions of import, handover, transport and recycling

To compare IFT-motor with IFT-train dynamics, we simultaneously monitored both kinesin-2 motors on IFT trains in a double-labelled strain (Supplementary Video 2). Anterograde IFT trains at the base and TZ were mainly occupied by kinesin-II motors (Fig. 2c), moving at ~0.5 μm s^{-1} (Fig. 2b) consistent with the

Table 1 Number of IFT proteins in wild type and IFT mutants.

IFT component (mutant background)	Base −0.50–0.25 μm	Transition zone 0.25–1.25 μm	Proximal segment 1.25–4.50 μm	Distal segment 4.50–7.50 μm	Total cilium 0.25–7.50 μm	Total cilium + base −0.50–7.50 μm	Number of phasmid cilia
IFT-A	474 ± 29	386 ± 19	802 ± 32	707 ± 32	**1,895 ± 49**	**2,369 ± 57**	50
IFT-B	845 ± 51	816 ± 40	1,709 ± 57	1,398 ± 65	**3,924 ± 95**	**4,769 ± 108**	52
Kinesin-II	241 ± 23	285 ± 20	204 ± 13	0	**489 ± 24**	**730 ± 33**	30
OSM-3	48 ± 2	52 ± 2	288 ± 9	440 ± 17	**781 ± 19**	**829 ± 19**	32
IFT-A (*kap-1*)	524 ± 30	271 ± 18	584 ± 22	505 ± 23	**1,360 ± 36**	**1,884 ± 47**	44
	+11 ± 8%	−30 ± 8%	−27 ± 5%	−29 ± 6%	−28 ± 4%	−20 ± 3%	
IFT-B (*kap-1*)	868 ± 53*	548 ± 38	1,133 ± 35	948 ± 46	**2,629 ± 69**	**3,497 ± 87**	40
	+3 ± 9%	−33 ± 8%	−34 ± 5%	−32 ± 7%	−33 ± 4%	−27 ± 3%	
Kinesin-II (*mksr-1*)	236 ± 14*	239 ± 19	282 ± 18	4 ± 3	**525 ± 26**	**761 ± 29**	42
	−2 ± 11%	−16 ± 11%	+38 ± 9%	–	+7 ± 7%	+4 ± 6%	
OSM-3 (*kap-1*)	110 ± 6	76 ± 5	316 ± 12	374 ± 20	**766 ± 24**	**877 ± 25**	46
	+129 ± 7%	+45 ± 8%	+10 ± 5%	−15 ± 7%	−2 ± 4%	+6 ± 4%	

Data obtained by quantification of the average cilium-intensity profile obtained from multiple phasmid cilia (right column). Top four rows: number of IFT-A, IFT-B, kinesin-II and OSM-3 for different ciliary regions in wild type. Bottom four rows: number of IFT-A, IFT-B, kinesin-II and OSM-3 in different mutant backgrounds; each of these rows is followed by a row indicating the difference between mutant and corresponding wild type (+, increase; −, decrease). Asterisks indicate that the average is statistically not different from wild type ($P > 0.01$ (unpaired two-tailed Student *t*-test)). All other comparisons are statistically different ($P < 0.01$ (unpaired two-tailed Student *t*-test)). Bold numbers represent total number of proteins in cilium (TZ, PS and DS) or cilium + base. All numbers: mean ± s.d. For number of worms and phasmid cilia imaged see Supplementary Fig. 6a–h; for IFT-A *kap-1* 22 worms and 44 phasmid cilia were imaged.

motor distribution (Fig. 1), but as they move along the PS, their motor composition changes as OSM-3 steadily replaces kinesin-II (Fig. 2c). This defines a previously undetected 'handover zone' along the PS, between 1 and 4 μm from the base, where IFT trains are transferred from the slower kinesin-II to the faster OSM-3, resulting in gradual acceleration of the IFT trains. This zone coincides with the location where IFT trains 'splay apart' (Fig. 2b,c and Supplementary Fig. 2a), suggesting that stochastic differences in kinesin-II/OSM-3 motor ratio might produce the different IFT-train velocities observed there[10]. Throughout the exchange process, OSM-3 motors become increasingly dominant, finally acting alone (Fig. 2c) to propel IFT trains at ∼1.5 μm s^{-1} along the DS (Fig. 2b and Supplementary Fig. 2a).

These data, together with data from *osm-3* and *kap-1* mutants (see below), show that kinesin-II or OSM-3, in the absence of its partner, moves IFT trains at approximately its *in vitro* velocity, that is, ∼0.5 μm s^{-1} and ∼1.5 μm s^{-1}, respectively[10,25,35,36]. However, the steady increase in IFT-train velocity, reflecting the gradually changing kinesin-2 motor composition as both motors move the same cargo along the PS (Fig. 2c,d), differs from the constant intermediate velocity of 0.7 μm s^{-1} observed previously[9,10]. Moreover, the functional form of this velocity increase (Fig. 2e) does not match previous competitive *in vitro* gliding assays using kinesin-2 mixtures, or the 'alternating action' and 'mechanical competition' models that fit the *in vitro* motor fraction–velocity curves[10], suggesting that additional factors may influence motor behaviour *in vivo*. To test this, we employed a variant of the alternating action model, the 'biased contribution' model, in which a 'bias parameter', γ, redistributes the motor contributions in response to, for example, motor regulation and force-dependent detachment (see 'Modelling of the motor-fraction train-velocity relation' in Methods). This model fits the data, yielding a γ of 9.6 ± 2, indicating that, *in vivo*, kinesin-2 motor activity is biased, with OSM-3 outcompeting kinesin-II tenfold while moving IFT trains along the handover zone. How OSM-3 activity is enhanced relative to kinesin-II is unknown but it could involve forward-load-induced shortening of kinesin-II run length[40].

In the retrograde direction, dynein-driven IFT trains moving along the DS contain only OSM-3 motors as cargo, but along the PS, OSM-3 is gradually replaced by kinesin-II (Fig. 2f). These motors are moved as cargo at rates matching dynein-driven IFT rafts (Supplementary Fig. 2b,c,e). This differs from *Chlamydomonas* where transport of kinesin-2 by retrograde IFT trains has not been observed, possibly because only a single kinesin-2 motor operates and retrograde transport is not required to maintain its spatial distribution[41–43]. We propose that in *C. elegans*, the elaborate IFT dynamics ensure that the kinesin-2 motors are confined to the ciliary regions where they exert their differentiated functions, maintaining kinesin-II around the cilium base and OSM-3 along the distal segment with the handover zone in between.

Single molecules of kinesin-II, OSM-3 and IFT-particle subcomplexes turn around at different ciliary regions

Motors and their cargo are thought to reverse direction at discrete 'turnaround locations', for example, the base and tip of the axoneme[1]. However, the kinesin-2 behaviour described above suggests that individual kinesin-II motors reverse direction throughout the handover zone, whereas OSM-3 might do so at more distal sites. To test this, we tracked individual kinesin-2 motors undergoing single-motor turnarounds in strains expressing KAP-1::eGFP, KAP-1::paGFP and OSM-3::paGFP (Fig. 3a). We observed kinesin-II motors undergoing sudden anterograde-to-retrograde turnarounds with no detectable intervening pauses (with time resolution 0.15 s), which were most frequent in the TZ and decreased along the PS, and then being transported back to the ciliary base as 'passengers' on IFT-dynein-driven trains (Fig. 3b,c and Supplementary Fig. 3a and Supplementary Videos 3 and 4). Retrograde-to-anterograde turnarounds, in contrast, occurred mainly at the ciliary base after a significant pause, lasting 1.4 ± 0.3 s (mean ± s.e.m., $n = 11$ single molecules pooled from 12 worms, 15 phasmid cilia; Fig. 3d,e and Supplementary Fig. 3b and Supplementary Videos 3 and 4). OSM-3 anterograde-to-retrograde turnarounds occurred along the DS, especially at the tip (Fig. 3f,g and Supplementary Fig. 3c) whereas retrograde-to-anterograde turnarounds were most frequent

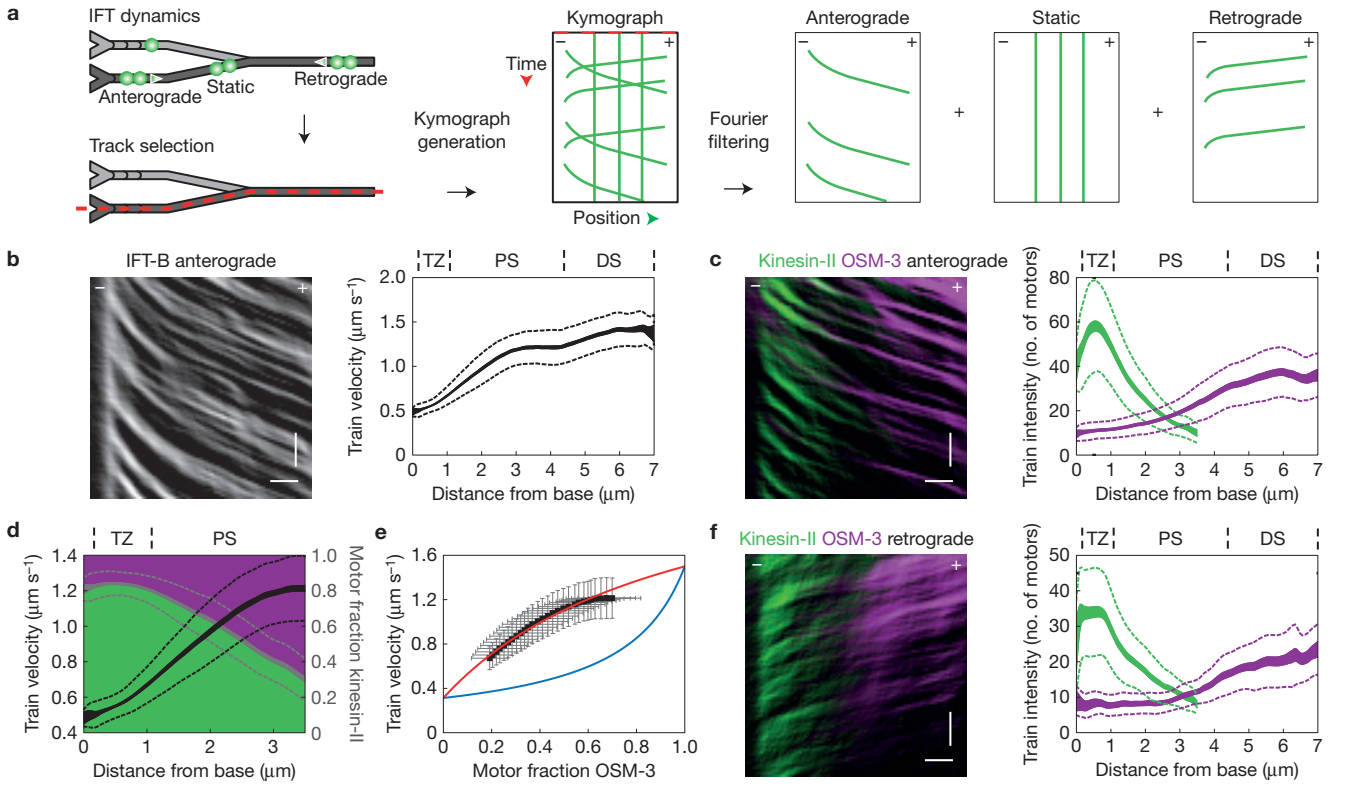

Figure 2 Kinesin-2 motors cooperate to transport IFT trains along cilia. (**a**) Kymographs are generated from image stacks by plotting subsequent intensity profiles obtained from lines drawn along cilia of interest (red dashed line). Kymographs are Fourier filtered to separate anterograde-moving, static, and retrograde-moving components. Subsequent automated analysis yields position-dependent average train intensities and velocities. (**b**) Representative anterograde Fourier-filtered kymograph of IFT-B-particle subcomplexes and corresponding train velocity. (**c**) Representative anterograde Fourier-filtered kymograph (from 44 worms, 88 phasmid cilia) of kinesin-II (green) and OSM-3 (magenta) with corresponding train intensity. (**d**) IFT-train velocity (from **b**) and kinesin-2 motor fraction, kinesin-II (green) and OSM-3 (magenta). (**e**) IFT-train velocity and OSM-3 motor fraction (from **d**, excluding the TZ, mean ± s.d.; black). Superimposed is the best fit with the biased contribution model (red) having an R^2 of 0.98 and γ of 9.6 ± 2. The motor-fraction train-velocity relation according to the alternating action model (blue; in agreement with the *in vitro* data[10]; using the kinesin-II velocity (0.31 μm s^{-1}) obtained from the fit of the biased contribution model (red)). In both cases the OSM-3 velocity was fixed at 1.5 μm s^{-1} (the maximum OSM-3 wild-type velocity measured (Fig. 5c)). (**f**) Representative retrograde Fourier-filtered kymograph (from 44 worms, 88 phasmid cilia) of kinesin-II (green) and OSM-3 (magenta) with corresponding train intensity. (**a**–**d**,**f**) Minus (−) and plus (+) denote microtubule polarity; horizontal scale bars, 1 μm; vertical scale bars, 2 s. Dashed lines represent mean ± s.d., line thickness represents 95% confidence interval for the mean (CIM). For number of kymograph trajectories included and number of worms imaged to obtain representative kymographs, see Supplementary Fig. 6a,c,d.

along the PS and TZ (Fig. 3h,i and Supplementary Fig. 3d). This behaviour ensures that kinesin-2 motors either act as 'drivers' of anterograde IFT trains or as 'passengers' on retrograde IFT trains spending little time detached, consistent with the steep kinesin-2 concentration gradients (Supplementary Fig. 1). All IFT-B anterograde-to-retrograde turnarounds occurred at the distal tip (16 out of 20 IFT-B-particle subcomplexes (with 4 being photobleached) pooled from 10 worms, 20 phasmid cilia; Supplementary Fig. 3e,f), whereas no retrograde-to-anterograde turnarounds were observed (27 IFT-B-particle subcomplexes pooled from 8 worms, 15 phasmid cilia). This suggests that IFT rafts perform a single run to the tip and back, and then 'disappear' in the cytoplasm, possibly owing to degradation or disassembly, in contrast to the kinesins, which are rapidly recycled to perform multiple runs back and forth.

Linking single-motor dynamics to motor distribution

To understand how single-motor dynamics underlie the time-averaged kinesin-2 motor distributions, we performed stochastic simulations with the IFT-train velocity defining the position-dependent single-motor velocities. A single motor was simulated to step and undergo multiple stochastic turnarounds (see 'Simulations of single-motor dynamics underlying ciliary distribution' in Methods), yielding turnaround distributions and time-averaged intensity profiles. For kinesin-II, the *in vivo* data could be described assuming constant turnaround probability (per unit time or space) in both directions and a 1.4 s pause during retrograde-to-anterograde turnaround (Fig. 4a). In our minimal model, differences in structure (for example, at the base and TZ) are represented only by the IFT-velocity profile. This could explain why the modelled intensity profile is narrower than the measured profile. In contrast, a representation of the OSM-3 data could be obtained only by assuming position-dependent turnaround probabilities, with retrograde-to-anterograde and anterograde-to-retrograde turnarounds having highest probability at tip and base, respectively (Fig. 4b). Our simulations show that the kinesin-2 distributions and turnaround positions can be described using turnaround probabilities, pause

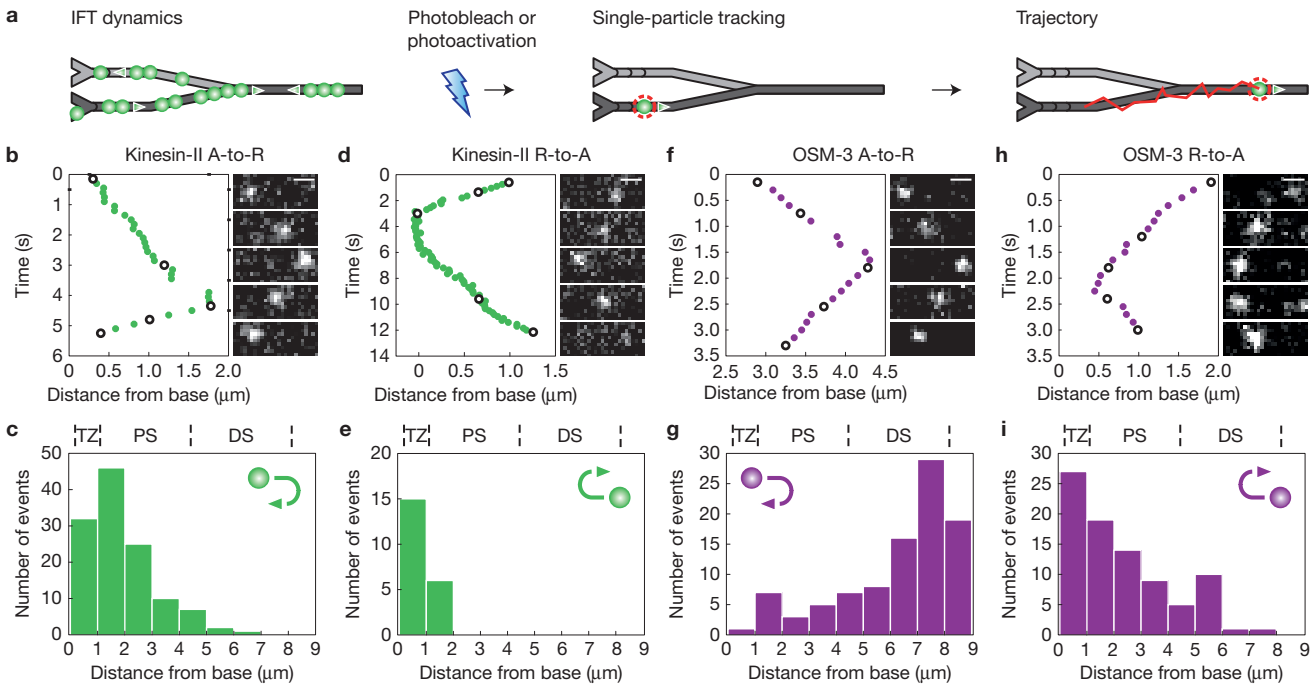

Figure 3 Single-motor turnarounds result in confinement of kinesin-II close to the base and OSM-3 near the distal segment. (**a**) Using photobleaching (eGFP) or photoactivation (paGFP) single-molecule imaging conditions can be reached at which single-motor trajectories can be obtained. (**b**–**i**) Representative single-motor trajectories (**b**,**d**,**f**,**h**, left), corresponding images (**b**,**d**,**f**,**h**, right, indicated by open symbols in trajectories) and histograms (**c**,**e**,**g**,**i**) of the locations of single-motor turnarounds for kinesin-II anterograde-to-retrograde (A-to-R) turnarounds ($n = 123$ single molecules pooled from 12 worms, 15 phasmid cilia) (**b**,**c**); for kinesin-II R-to-A turnarounds ($n = 21$ single molecules pooled from 12 worms, 15 phasmid cilia) (**d**,**e**); OSM-3 A-to-R turnarounds ($n = 95$ single molecules pooled from 20 worms, 31 phasmid cilia) (**f**,**g**); and OSM-3 R-to-A turnarounds ($n = 86$ single molecules pooled from 20 worms, 31 phasmid cilia) (**h**,**i**). Scale bars, 0.5 μm. Representative turnaround trajectories and corresponding images were selected from the data set indicated above.

durations and velocities as input parameters, revealing important differences between the kinesin-2 turnaround probabilities. The highly position-dependent turnaround probability of OSM-3 indicates that OSM-3 detachment is tightly regulated in a position-dependent manner.

Kinesin-II and OSM-3 facilitate ciliary import and long-range transport, respectively

IFT assays in motor mutants further illuminated the functional significance of kinesin-2 motor cooperation. In mutants lacking kinesin-II function, we observed a redistribution of OSM-3, which accumulated in front of the TZ and was depleted from the DS (Fig. 5a and Supplementary Fig. 4a,b and Table 1). The increased accumulation at the base apparently allows twofold more OSM-3 to dock onto anterograde IFT trains that subsequently move along the TZ and PS compared with wild type (Supplementary Fig. 4c,d). Significantly, in contrast to the gradual acceleration observed in wild type, OSM-3 and anterograde IFT trains entered the cilium in delayed bursts and immediately reached their maximal velocity (Fig. 5b,c and Supplementary Fig. 4c and Supplementary Video 5). In mutants lacking OSM-3 function, kinesin-II motors redistributed to become slightly more abundant around the TZ and were absent from the terminal region of the PS (Fig. 5d). Kinesin-II entry into the cilium seemed to be unaffected but the motors seemed to move in diffuse clouds associated with less well-defined trains compared with wild type, indicating an effect on IFT-train organization (Fig. 5e and Supplementary Video 6 and Supplementary Fig. 4e). Intriguingly, we detected no individual kinesin-II motors further than ~3 μm from the base (Fig. 5f), suggesting that OSM-3 motors in the handover zone normally pull the kinesin-II motors further along the PS than they travel by themselves. This suggests that kinesin-II, acting alone, cannot move as far as the DS so its function is restricted to the region around the ciliary base and TZ, for example, cargo import, leaving OSM-3 to drive long-distance transport to the distal tip of the axoneme.

Transition-zone structures act as roadblocks affecting IFT dynamics

The TZ is characterized by Y-shaped axoneme-membrane crosslinkers that control ciliary import–export (Fig. 1a)[20]. Its organization is disrupted by mutations[44] that cause ciliopathies, for example, nephronophthisis and Meckel–Gruber syndrome[20] (MKS). To test the effect of these structures on the import and transport functions of kinesin-II, we used an MKS-1-related protein 1 (MKSR-1) mutant (*mksr-1*) and confirmed that it has defective TZs lacking MKS-6 (ref. 44; Supplementary Figs 4f and 1a). In these mutants, kinesin-II motors became redistributed, being reduced in the TZ and correspondingly enhanced in the PS (Fig. 5g and Supplementary Fig. 4g and Table 1) and IFT-train dynamics were significantly altered, whereas ciliary entry was not substantially affected (Fig. 5h and

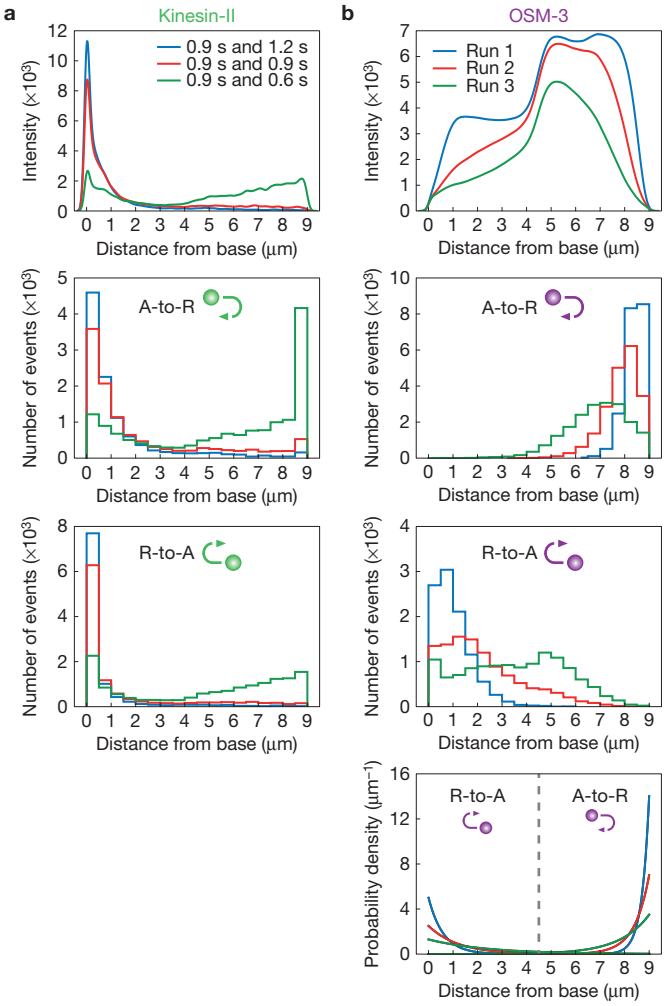

Figure 4 Stochastic simulations of single-motor dynamics reveal the effect of turnaround probability on kinesin-2 distribution. (**a**) Simulations for kinesin-II. Top panel: time-averaged intensity profiles. Lower two panels: histograms of the locations of single-motor turnarounds. Simulations were performed with a constant turnaround probability per unit time. Blue traces: A-to-R turnaround time constant 0.9 s, R-to-A 1.2 s. Red traces: A-to-R turnaround time constant 0.9 s, R-to-A 0.9 s. Green traces: A-to-R turnaround time constant 0.9 s, R-to-A 0.6 s. (**b**) Simulations for OSM-3. Top panel: time-averaged intensity profiles. Middle two panels: histograms of the locations of single-motor turnarounds. Lower panel: position-dependent turnaround probability densities used for simulations. Defined by: $0.014e^{(x-9{,}000)/300}$, $0.007e^{(x-9{,}000)/600}$ and $0.0035e^{(x-9{,}000)/1{,}200}$ for A-to-R Run 1, 2 and 3, respectively. Defined by: $0.005e^{-x/600}$, $0.0025e^{-x/1{,}200}$ and $0.0013e^{-x/2{,}400}$ for R-to-A Run 1, 2 and 3, respectively. Note that for each simulation run both A-to-R and R-to-A probability densities are shown. (**a**,**b**) Red traces represent simulations that describe experimental data best.

Supplementary Video 7). In fact, IFT trains moved faster through the TZ but seemed to move slower along the PS, compared with wild type (Fig. 5i), accounting for the kinesin-II redistribution (Fig. 5g and Table 1) and explaining why anterograde IFT trains contain more kinesin-II motors in the handover zone (Fig. 5h). We propose that kinesin-II encounters fewer obstacles in *mksr-1* mutants, moving faster through the TZ and therefore progressing further along the PS. Retrograde IFT trains slowed down much closer to the base than in wild-type animals (Fig. 5j), which supports the roadblock hypothesis. Finally, we observed that OSM-3, which normally has difficulty traversing the TZ in the absence of kinesin-II, traverses the TZ more easily in *kap-1;mksr-1* double mutants where IFT trains exhibited accelerated transport (Fig. 5k) and entry events occurred without delay (Supplementary Fig. 4h). These results suggest that protein roadblocks may partially confine kinesin-II to the TZ where it slowly navigates IFT trains around these obstacles before handing off its cargo to OSM-3, which then drives long-distance transport to the ciliary tip.

Kinesin-II mediates both loading and transport at the TZ

Ciliary import of the IFT machinery and associated cargo is thought to involve its docking to the periciliary membrane, followed by passage through the base (loading) and TZ (transport)[19]. To investigate the role of kinesin-2 motors in this process, we examined the transport of IFT-particle subcomplexes in strains containing or lacking kinesin-II function. Remarkably, in the presence versus the absence of kinesin-II function, the number of IFT-particle subcomplexes (IFT-A and IFT-B) inside the cilium was about twofold higher but the number at the ciliary base was similar (Fig. 6a and Supplementary Fig. 5a and Table 1), indicating that proper loading of the IFT machinery requires kinesin-II function. Accordingly, following loss of kinesin-II function: IFT frequency decreased (Fig. 6b,c), leading to a higher coefficient of variation in kymographs of IFT-A and IFT-B (Supplementary Fig. 5b,c); fewer IFT-particle subcomplexes assembled into IFT trains, resulting in their accumulation in front of the TZ (Fig. 6d,e); and IFT-particle-subcomplex passage through the base took more than twofold longer (Fig. 6f), whereas TZ escape times were similar (Supplementary Fig. 5d). Thus, kinesin-II increases the number of IFT-particle subcomplexes inside the ciliary compartment by shortening the time they take to load into the TZ. Altogether, these results suggest a functional differentiation in which the slower, less processive, kinesin-II functions as an import motor at the base, capable of effectively navigating the TZ. In contrast, the faster, more processive OSM-3 has difficulty negotiating the TZ and instead functions as a long-range transporter of IFT trains to the ciliary tip.

DISCUSSION

Previous IFT assays[45,46] suggested that kinesin-II and OSM-3 motors move IFT trains at a constant intermediate velocity to build the PS in a redundant fashion but the reason was unclear[9,10,34]. Our work reveals a functional differentiation between kinesin-II and OSM-3 that optimizes cargo delivery. Thus, kinesin-II serves primarily as an 'import' motor at the structurally dense ciliary base and TZ, where it may use its ability to switch tracks under load[47] and to navigate IFT trains around roadblocks[48]. Significantly, the TZ corresponds to the 'connecting cilium' of vertebrate photoreceptors where the heterotrimeric kinesin-2-driven transport of opsins and axoneme precursors is under intense scrutiny[49,50]. In contrast, the faster, more processive OSM-3 serves as a long-range 'transport' motor along the relatively obstacle-free DS track to deliver IFT trains to the ciliary tip. Future *in vitro* motility experiments on individual kinesin-2 motors and well-defined motor assemblies will be needed to further dissect their cooperative behaviour and to investigate if kinesin-II and OSM-3 respond differently to roadblocks.

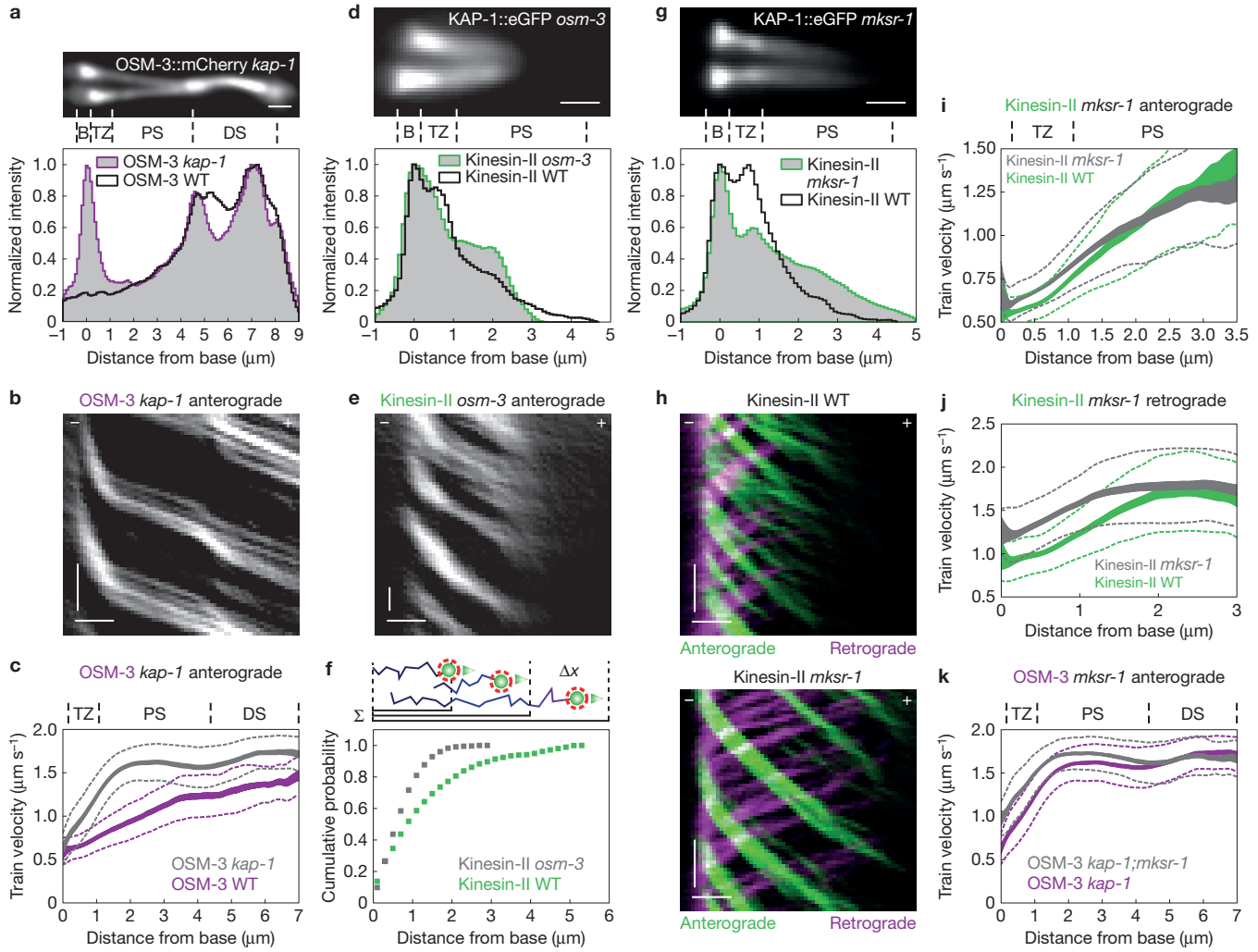

Figure 5 Mutants with IFT defects reveal kinesin-2 functional specialization. (**a**–**c**) OSM-3 in a kinesin-II loss-of-function mutant (*kap-1*). (**a**) Representative time-averaged fluorescence image (top); corresponding fluorescence-intensity profile (bottom) along upper cilium (grey) with OSM-3 wild-type profile (black; Fig. 1e). (**b**) Representative anterograde Fourier-filtered kymograph. (**c**) OSM-3 anterograde train velocity (grey); wild type shown in magenta. (**d**–**f**) Kinesin-II in an *osm-3* mutant. (**d**) Representative time-averaged fluorescence image (top, from 12 worms, 24 phasmid cilia); corresponding fluorescence-intensity profile (bottom) along lower cilium (grey) with the kinesin-II wild-type profile (black; Fig. 1d). (**e**) Representative anterograde Fourier-filtered kymograph (from 12 worms, 24 phasmid cilia). (**f**) Cumulative probability distributions of anterograde-moving kinesin-II in strains lacking (grey, $n = 189$ trajectories, from 43 worms, 68 phasmid cilia) and containing OSM-3 (green, $n = 120$ trajectories, from 20 worms, 34 phasmid cilia). Distributions represent summed (Σ) probabilities of finding a kinesin-II within a certain distance (Δx) from the base (top). (**g**–**k**) Kinesin-II in an *mksr-1* mutant. (**g**) Representative time-averaged fluorescence image (top); corresponding fluorescence-intensity profile (bottom) along lower cilium (grey) with kinesin-II wild-type profile (black; Supplementary Fig. 1a). (**h**) Representative anterograde (green) and retrograde (magenta) Fourier-filtered kymographs (top, wild type; bottom, *mksr-1* mutant). In the handover zone (at 3.5 μm from the base) 56 ± 12% more kinesin-II motors are present on IFT trains in the *mksr-1* mutant compared with wild type (mean ± s.e.m.; wild type: $n = 34$ IFT trains, from 15 worms, 30 phasmid cilia; *mksr-1* mutant: $n = 68$ IFT trains, from 22 worms, 42 phasmid cilia). Kymographs obtained and represented with identical settings. (**i**,**j**) Anterograde (**i**) and retrograde (**j**) velocities of kinesin-II in wild type (green) and *mksr-1* mutant (grey). (**k**) Anterograde velocity of OSM-3 in a kinesin-II (*kap-1*, purple) and kinesin-II MKSR-1 double mutant (*kap-1*;*mksr-1*, grey). (**a**,**d**,**g**) Scale bars, 1 μm. Fluorescence-intensity profiles normalized to their maxima (OSM-3 intensity comparison in Supplementary Fig. 4a). (**b**,**e**,**h**) Minus (−) and plus (+) denote microtubule polarity; horizontal scale bars, 1 μm; vertical scale bars, 2 s. (**c**,**i**–**k**) Dashed lines, means ± s.d.; line thickness: 95% CIM. For number of kymograph trajectories included and worms imaged to obtain representative images, see Supplementary Fig. 6c–g.

When either motor operates alone, it moves IFT trains at rates matching those measured *in vitro*[10,35,36]. However, the handover of the IFT trains from kinesin-II to OSM-3 creates a gradual increase in velocity distinct from the constant intermediate velocity seen along the PS and the mole fraction–velocity curves observed *in vitro* previously[9,10]. A biased contribution model with OSM-3 outcompeting kinesin-II by a factor of ~10 fits the train-velocity versus motor-ratio curves. This may reflect additional regulatory factors that are absent *in vitro*, for example, tubulin post-translational modifications that affect kinesin-2 velocity[51]. Our results seem relevant to the debate over whether teams of multiple, same-polarity motors bound to a single cargo act independently, interfere with one another, or function

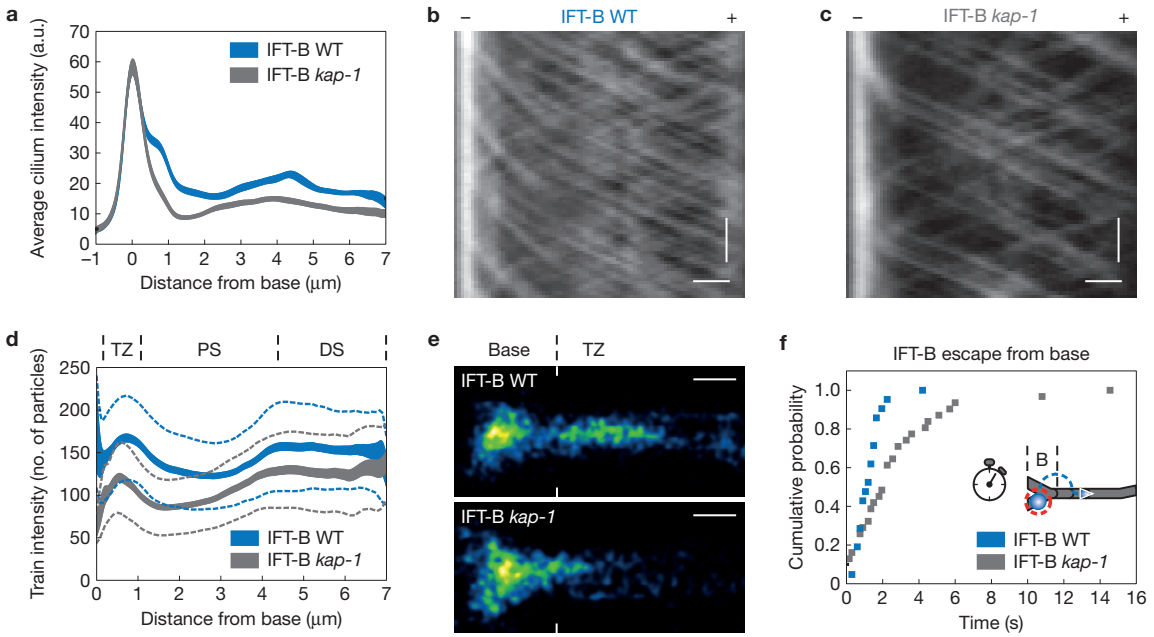

Figure 6 IFT-particle-subcomplex loading and distribution is altered in the absence of kinesin-II. (**a**) Average fluorescence-intensity profiles obtained from time-averaged fluorescence images (22.5 s each) of multiple different phasmid cilia. IFT-B in kinesin-II mutant background (*kap-1*, grey) pooled from 17 worms, 40 phasmid cilia, and wild-type IFT-B (blue) pooled from 19 worms, 52 phasmid cilia. (**b**,**c**) Representative kymograph obtained from an image stack of IFT-B in *C. elegans* strains containing (**b**) and lacking (**c**) functional kinesin-II. (**d**) Average IFT-B intensity for anterograde trains in *C. elegans* strains lacking (grey) and containing (blue) functional kinesin-II. (**e**) Representative super-resolution images obtained by accumulating localizations of multiple single-molecule trajectories for IFT-B in *C. elegans* strains containing (top; from 10 worms, 19 phasmid cilia) and lacking (bottom; from 25 worms, 38 phasmid cilia) functional kinesin-II (see also Supplementary Fig. 6k). Scale bars, 0.25 μm. (**f**) Cumulative probability distribution of the durations of single-particle subcomplexes escaping from the base. Distributions are obtained by defining a region of interest and measuring the time it takes for a particle subcomplex to cross the boundary in the anterograde direction (inset). IFT-B-particle subcomplexes escaped the base in 1.3 ± 0.2 s (mean ± s.e.m., n=21 IFT-B-particle subcomplexes from 10 worms, 19 phasmid cilia) in the presence of kinesin-II and in 2.9 ± 0.6 s (mean ± s.e.m., n=31 IFT-B-particle subcomplexes from 25 worms, 38 phasmid cilia) in the absence of functional kinesin-II. (**b**,**c**) Minus (−) and plus (+) denote microtubule polarity; horizontal scale bars, 1 μm; vertical scale bars, 2 s. Dashed lines are mean ± s.d.; line thickness represents 95% CIM. For number of kymograph trajectories included and number of worms imaged to obtain representative kymographs, see Supplementary Fig. 6a,h).

in a coordinated fashion[8,11–14]. Moreover, the gradual handover produces far richer dynamic behaviour than the mono- and biphasic velocity reported previously for *C. elegans*[9] and *Chlamydomonas*[15,16] and resembles the complex dynamics seen in cilia of, for example, trypanosomes[52] and mouse olfactory neurons[53]. The functional cooperation between distinct anterograde motors, which coexist in many cilia, could contribute to such complex IFT dynamics[37,38].

The functional differentiation between kinesin-II and OSM-3 depends on IFT dynamics, which defines the motors' distinct spatial distributions. At the transition zone, IFT trains are occupied by kinesin-II, which gradually undocks during anterograde transport and is replaced by OSM-3. Conversely, as retrograde IFT trains are recycled back to the ciliary base, the OSM-3/kinesin-II motor ratio gradually changes from being mainly OSM-3 to being mainly kinesin-II (ref. 30). Our simulations indicate that this depends on interplay between train-velocity and motor-turnaround probability, with kinesin-II turnaround being relatively constant along the cilium and that of OSM-3 being enhanced at both ends. This could possibly indicate the operation of unknown regulatory mechanisms that also might contribute to the bias parameter, for example, cargo-dependent relief of autoinhibition[36], specific kinases that influence kinesin-2 docking and undocking[54,55], ciliary proteins required for kinesin-2 coordination[31] and cues from the axonemal track such as distinct tubulin isotypes and the Y-shaped linkers of the TZ that could influence kinesin-2 motility[56,57].

Our view of kinesin-2 collaboration also raises questions. For example, we find that, in the absence of OSM-3 function, kinesin-II cannot reach the tip of the PS yet it can still build the PS (refs 9,32,34). Perhaps a small but sufficient number of undetected kinesin-II motors do make it to the end of the PS, or perhaps diffusion contributes to the final stages of PS precursor delivery. Similarly, in the absence of kinesin-II function, OSM-3 can build a full-length cilium[9,34] despite our observation of significant loading delays. Perhaps further work will reveal subtle defects in such mutants, for example, failure to properly localize specific ciliary signalling molecules.

We propose that the functional differentiation of kinesin-II and OSM-3 into an import motor and transport motor, respectively, optimizes sequential steps of anterograde IFT to build the cilium. The system thus exploits each kinesin-2's specific motor properties and requires that the number of motors on the cargo, that is, the IFT train, is well orchestrated, resulting in a gradual exchange of the different motors to ensure reliable handover of cargo (Fig. 7). In a broader context, the deployment of similar, same-polarity yet functionally differentiated motors may represent a common strategy for optimizing intracellular transport. □

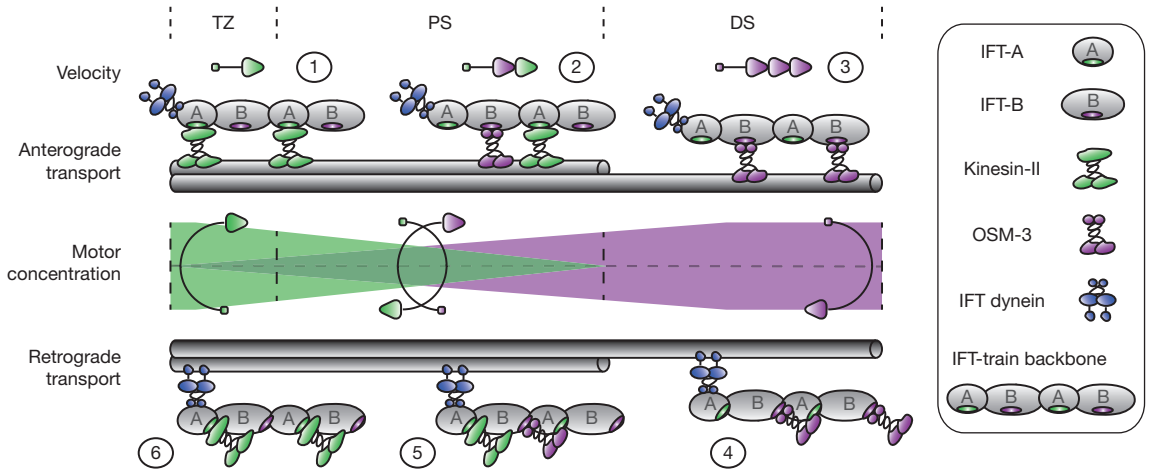

Figure 7 'Gradual handover' as a mode of action for same-polarity motor-protein cooperation. Cartoon model. (1) A stable IFT-train backbone (consisting of IFT-A and IFT-B-particle subcomplexes) is loaded into the cilium and transported through the transition zone (TZ) at ~0.5 μm s^{-1} mainly by kinesin-II. (2) After navigating the TZ, kinesin-II gradually undocks while, at the same time, OSM-3 motors start docking, resulting in a gradually accelerating IFT train reaching ~1.3 μm s^{-1} at the end of the proximal segment (PS), and ensuring reliable handover of the backbone. (3) In the distal segment (DS), the train is occupied solely by OSM-3 reaching a terminal velocity of ~1.5 μm s^{-1}. (4) Following turnaround and remodelling at the ciliary tip, the backbone is returned to the base by IFT dynein, recycling OSM-3. (5) OSM-3 undocks from retrograde IFT trains along the PS, while kinesin-II gradually docks. (6) Close to the base, kinesin-II is the main kinesin cargo of retrograde IFT trains. In this way, the complete IFT-system dynamics ensure enrichment of kinesin-II at the base and TZ and of OSM-3 in the DS. For clarity, only a limited number of IFT-particle subcomplexes and motors are represented. Our measurements (see Fig. 2 and Supplementary Fig. 2) indicate that anterograde trains contain on average ~60 IFT-A and ~150 IFT-B-particle subcomplexes, with kinesin-II motor number decreasing from ~50 to ~0 and OSM-3 motor number increasing from ~10 to ~40. Retrograde trains contain on average ~40 IFT-A and ~80 IFT-B-particle subcomplexes, with kinesin-II motor number increasing from ~0 to ~30 and OSM-3 motor number decreasing from ~20 to ~10.

METHODS

Methods and any associated references are available in the online version of the paper.

Note: Supplementary Information is available in the online version of the paper

ACKNOWLEDGEMENTS

During initial stages of the project, B.P. was a visiting student in the Scholey Laboratory, Department of MCB at UC Davis. We thank S. Açar, L. Hao (UC Davis), D. Cheerambathur and A. Desai (UC San Diego) for discussion; S. Mitani (NPB, Japan) for the *tm3433* deletion mutant; E. Kroezinga for biochemical support; P. Noordeloos for technical support; J. Girard and J. Mijalkovic for critical reading of the manuscript (VU University Amsterdam). Some strains were provided by the CGC, which is funded by NIH Office of Research Infrastructure Programs (P40 OD010440). We acknowledge financial support from the Netherlands Organisation for Scientific Research (NWO) via a Vici, an NWO-Groot and an ALW Open Program grant, via the STW research programme 'Nanoscopy', the FOM programme 'Barriers in the Brain', a grant from NanoNextNL of the Government of the Netherlands and 130 partners (E.J.G.P.), and from an NIH grant no. GM50718 (J.M.S.).

AUTHOR CONTRIBUTIONS

B.P., J.M.S. and E.J.G.P. initiated research. B.P. created reagents. B.P. and E.J.G.P. designed experiments. B.P., P.M. and F.O. performed experiments and analysed data. All authors contributed to data interpretation, with P.M. particularly contributing to the simulations and kymograph analysis and F.O. to the single-molecule analysis. B.P., J.M.S. and E.J.G.P. wrote the manuscript. All authors read the manuscript.

COMPETING FINANCIAL INTERESTS

The authors declare no competing financial interests.

Published online at http://dx.doi.org/10.1038/ncb3263
Reprints and permissions information is available online at www.nature.com/reprints

1. Vale, R. D. The molecular motor toolbox for intracellular transport. *Cell* **112,** 467–480 (2003).
2. Hirokawa, N., Noda, Y., Tanaka, Y. & Niwa, S. Kinesin superfamily motor proteins and intracellular transport. *Nat. Rev. Mol. Cell Biol.* **10,** 682–696 (2009).
3. Scholey, J. M. Kinesin-2: a family of heterotrimeric and homodimeric motors with diverse intracellular transport functions. *Annu. Rev. Cell Dev. Biol.* **29,** 443–469 (2013).
4. Encalada, S. E. & Goldstein, L. S. Biophysical challenges to axonal transport: motor-cargo deficiencies and neurodegeneration. *Annu. Rev. Biophys.* **43,** 141–169 (2014).
5. Hou, Y. Q. & Witman, G. B. Dynein and intraflagellar transport. *Exp. Cell Res.* **334,** 26–34 (2015).
6. Mallik, R., Rai, A. K., Barak, P., Rai, A. & Kunwar, A. Teamwork in microtubule motors. *Trends Cell Biol.* **23,** 575–582 (2013).
7. Jolly, A. L. & Gelfand, V. I. Bidirectional intracellular transport: utility and mechanism. *Biochem. Soc. Trans.* **39,** 1126–1130 (2011).
8. Derr, N. D. *et al.* Tug-of-war in motor protein ensembles revealed with a programmable DNA origami scaffold. *Science* **338,** 662–665 (2012).
9. Snow, J. J. *et al.* Two anterograde intraflagellar transport motors cooperate to build sensory cilia on *C. elegans* neurons. *Nat. Cell Biol.* **6,** 1109–1123 (2004).
10. Pan, X. Y. *et al.* Mechanism of transport of IFT particles in *C. elegans* cilia by the concerted action of kinesin-II and OSM-3 motors. *J. Cell Biol.* **174,** 1035–1045 (2006).
11. Rogers, A. R., Driver, J. W., Constantinou, P. E., Jamison, D. K. & Diehl, M. R. Negative interference dominates collective transport of kinesin motors in the absence of load. *Phys. Chem. Chem. Phys.* **11,** 4882–4889 (2009).
12. Bieling, P., Kronja, I. & Surrey, T. Microtubule motility on reconstituted meiotic chromatin. *Curr. Biol.* **20,** 763–769 (2010).
13. Furuta, K. *et al.* Measuring collective transport by defined numbers of processive and nonprocessive kinesin motors. *Proc. Natl Acad. Sci. USA* **110,** 501–506 (2013).
14. Norris, S. R. *et al.* A method for multiprotein assembly in cells reveals independent action of kinesins in complex. *J. Cell Biol.* **207,** 393–406 (2014).
15. Ishikawa, H. & Marshall, W. F. Ciliogenesis: building the cell's antenna. *Nat. Rev. Mol. Cell Biol.* **12,** 222–234 (2011).
16. Pedersen, L. B. & Rosenbaum, J. L. Intraflagellar transport (Ift): role in ciliary assembly, resorption and signalling. *Curr. Top. Dev. Biol.* **85,** 23–61 (2008).
17. Pigino, G. *et al.* Electron-tomographic analysis of intraflagellar transport particle trains *in situ*. *J. Cell Biol.* **187,** 135–148 (2009).
18. Cole, D. G. *et al. Chlamydomonas* kinesin-II-dependent intraflagellar transport (IFT): IFT particles contain proteins required for ciliary assembly in *Caenorhabditis elegans* sensory neurons. *J. Cell Biol.* **141,** 993–1008 (1998).
19. Nachury, M. V., Seeley, E. S. & Jin, H. Trafficking to the ciliary membrane: how to get across the periciliary diffusion barrier? *Annu. Rev. Cell Dev. Biol.* **26,** 59–87 (2010).
20. Reiter, J. F., Blacque, O. E. & Leroux, M. R. The base of the cilium: roles for transition fibres and the transition zone in ciliary formation, maintenance and compartmentalization. *EMBO Rep.* **13,** 608–618 (2012).

21. Bhogaraju, S. *et al.* Molecular basis of tubulin transport within the cilium by IFT74 and IFT81. *Science* **341,** 1009–1012 (2013).
22. Craft, J. M., Harris, J. A., Hyman, S., Kner, P. & Lechtreck, K. F. Tubulin transport by IFT is upregulated during ciliary growth by a cilium-autonomous mechanism. *J. Cell Biol.* **208,** 223–237 (2015).
23. Hao, L. M. *et al.* Intraflagellar transport delivers tubulin isotypes to sensory cilium middle and distal segments. *Nat. Cell Biol.* **13,** 790–453 (2011).
24. Marshall, W. F. & Rosenbaum, J. L. Intraflagellar transport balances continuous turnover of outer doublet microtubules: implications for flagellar length control. *J. Cell Biol.* **155,** 405–414 (2001).
25. Cole, D. G. *et al.* Novel heterotrimeric kinesin-related protein purified from sea-urchin eggs. *Nature* **366,** 268–270 (1993).
26. Walther, Z., Vashishtha, M. & Hall, J. L. The *Chlamydomonas* Fla10 gene encodes a novel kinesin-homologous protein. *J. Cell Biol.* **126,** 175–188 (1994).
27. Kozminski, K. G., Beech, P. L. & Rosenbaum, J. L. The *Chlamydomonas* kinesin-like protein Fla10 is involved in motility associated with the flagellar membrane. *J. Cell Biol.* **131,** 1517–1527 (1995).
28. Pazour, G. J., Dickert, B. L. & Witman, G. B. The DHC1b (DHC2) isoform of cytoplasmic dynein is required for flagellar assembly. *J. Cell Biol.* **144,** 473–481 (1999).
29. Porter, M. E., Bower, R., Knott, J. A., Byrd, P. & Dentler, W. Cytoplasmic dynein heavy chain 1b is required for flagellar assembly in *Chlamydomonas*. *Mol. Biol. Cell* **10,** 693–712 (1999).
30. Signor, D. *et al.* Role of a class DHC1b dynein in retrograde transport of IFT motors and IFT raft particles along cilia, but not dendrites, in chemosensory neurons of living *Caenorhabditis elegans*. *J. Cell Biol.* **147,** 519–530 (1999).
31. Ou, G. S., Blacque, O. E., Snow, J. J., Leroux, M. R. & Scholey, J. M. Functional coordination of intraflagellar transport motors. *Nature* **436,** 583–587 (2005).
32. Perkins, L. A., Hedgecock, E. M., Thomson, J. N. & Culotti, J. G. Mutant sensory cilia in the nematode *Caenorhabditis-elegans*. *Dev. Biol.* **117,** 456–487 (1986).
33. Starich, T. A. *et al.* Mutations affecting the chemosensory neurons of *Caenorhabditis elegans*. *Genetics* **139,** 171–188 (1995).
34. Evans, J. E. *et al.* Functional modulation of IFT kinesins extends the sensory repertoire of ciliated neurons in *Caenorhabditis elegans*. *J. Cell Biol.* **172,** 663–669 (2006).
35. Brunnbauer, M. *et al.* Regulation of a heterodimeric kinesin-2 through an unprocessive motor domain that is turned processive by its partner. *Proc. Natl Acad. Sci. USA* **107,** 10460–10465 (2010).
36. Imanishi, M., Endres, N. F., Gennerich, A. & Vale, R. D. Autoinhibition regulates the motility of the *C. elegans* intraflagellar transport motor OSM-3. *J. Cell Biol.* **174,** 931–937 (2006).
37. Verhey, K. J., Dishinger, J. & Kee, H. L. Kinesin motors and primary cilia. *Biochem. Soc. Trans.* **39,** 1120–1125 (2011).
38. Malicki, J. & Besharse, J. C. Kinesin-2 family motors in the unusual photoreceptor cilium. *Vision Res.* **75,** 33–36 (2012).
39. Ludington, W. B., Wemmer, K. A., Lechtreck, K. F., Witman, G. B. & Marshall, W. F. Avalanche-like behavior in ciliary import. *Proc. Natl Acad. Sci. USA* **110,** 3925–3930 (2013).
40. Milic, B., Andreasson, J. O. L., Hancock, W. O. & Block, S. M. Kinesin processivity is gated by phosphate release. *Proc. Natl Acad. Sci. USA* **111,** 14136–14140 (2014).
41. Engel, B. D. *et al.* The role of retrograde intraflagellar transport in flagellar assembly, maintenance, and function. *J. Cell Biol.* **199,** 151–167 (2012).
42. Pedersen, L. B., Gelmer, S. & Rosenbaum, J. L. Dissecting the molecular mechanisms of intraflagellar transport in *Chlamydomonas*. *Curr. Biol.* **16,** 450–459 (2006).
43. Mueller, J., Perrone, C. A., Bower, R., Cole, D. G. & Porter, M. E. The FLA3 KAP subunit is required for localization of kinesin-2 to the site of flagellar assembly and processive anterograde intraflagellar transport. *Mol. Biol. Cell* **16,** 1341–1354 (2005).
44. Williams, C. L. *et al.* MKS and NPHP modules cooperate to establish basal body/transition zone membrane associations and ciliary gate function during ciliogenesis. *J. Cell Biol.* **192,** 1023–1041 (2011).
45. Orozco, J. T. *et al.* Movement of motor and cargo along cilia. *Nature* **398,** 674 (1999).
46. Kozminski, K. G., Johnson, K. A., Forscher, P. & Rosenbaum, J. L. A motility in the eukaryotic flagellum unrelated to flagellar beating. *Proc. Natl Acad. Sci. USA* **90,** 5519–5523 (1993).
47. Schroeder, H. W. *et al.* Force-dependent detachment of kinesin-2 biases track switching at cytoskeletal filament intersections. *Biophys. J.* **103,** 48–58 (2012).
48. Hoeprich, G. J., Thompson, A. R., McVicker, D. P., Hancock, W. O. & Berger, C. L. Kinesin's neck-linker determines its ability to navigate obstacles on the microtubule surface. *Biophys. J.* **106,** 1691–1700 (2014).
49. Trivedi, D., Colin, E., Louie, C. M. & Williams, D. S. Live-cell imaging evidence for the ciliary transport of rod photoreceptor opsin by heterotrimeric kinesin-2. *J. Neurosci.* **32,** 10587–10593 (2012).
50. Jiang, L. *et al.* Heterotrimeric kinesin-2 (KIF3) mediates transition zone and axoneme formation of mouse photoreceptors. *J. Biol. Chem.* **290,** 12765–12778 (2015).
51. O'Hagan, R. *et al.* The tubulin deglutamylase CCPP-1 regulates the function and stability of sensory cilia in *C. elegans*. *Curr. Biol.* **21,** 1685–1694 (2011).
52. Buisson, J. *et al.* Intraflagellar transport proteins cycle between the flagellum and its base. *J. Cell Sci.* **126,** 327–338 (2013).
53. Williams, C. L. *et al.* Direct evidence for BBSome-associated intraflagellar transport reveals distinct properties of native mammalian cilia. *Nat. Commun.* **5,** 5813 (2014).
54. Burghoorn, J. *et al.* Mutation of the MAP kinase DYF-5 affects docking and undocking of kinesin-2 motors and reduces their speed in the cilia of *Caenorhabditis elegans*. *Proc. Natl Acad. Sci. USA* **104,** 7157–7162 (2007).
55. Liang, Y. W. *et al.* FLA8/KIF3B phosphorylation regulates kinesin-II interaction with IFT-B to control IFT entry and turnaround. *Dev. Cell* **30,** 585–597 (2014).
56. Verhey, K. J. & Hammond, J. W. Traffic control: regulation of kinesin motors. *Nat. Rev. Mol. Cell Biol.* **10,** 765–777 (2009).
57. Sirajuddin, M., Rice, L. M. & Vale, R. D. Regulation of microtubule motors by tubulin isotypes and post-translational modifications. *Nat. Cell Biol.* **16,** 335–344 (2014).
58. Wedaman, K. P., Meyer, D. W., Rashid, D. J., Cole, D. G. & Scholey, J. M. Sequence and submolecular localization of the 115-kD accessory subunit of the heterotrimeric kinesin-II (KRP(85/95)) complex. *J. Cell Biol.* **132,** 371–380 (1996).

DOI: 10.1038/ncb3263

METHODS

Fluorescence microscopy. Microscopic images were acquired using a custom-built epi-illuminated wide-field fluorescence microscope operated by a Micro-Manager software interface (μManager, Micro-Manager 1.4, https://www.micro-manager.org), built around an inverted microscope body (Nikon, Eclipse Ti) fitted with a 60× water-immersion objective (Nikon, CFI Plan Apo IR 60× WI, N.A.: 1.27). Excitation light, provided by two diode-pumped solid-state lasers (Cobolt Calypso 50 491 nm DPSS; and Cobolt Jive 50 561 nm DPSS), was first passed through an AOTF (AA Opto-Electronics, AOTFnC-400.650-TN) for wavelength selection, next through a quarter-wave plate (Thorlabs, mounted achromatic quarter-wave plate, 400–800 nm, AQWP05M-600) to obtain circularly polarized light, and finally through a diffuser (SUSS MicroOptics, rotating ground-glass diffuser (tilted version), $1° \pm 0.25°$ full-width at half-maximum at 650 nm, AR-coating 400–750 nm $R < 0.5\%$, double-sided) to obtain uniform illumination, before being coupled into the objective using a dichroic mirror (Semrock, 488/561 nm lasers Brightline dual-edge laser-flat, Di01-R488/561-25×36). Emission light was separated using a dichroic long-pass filter (Chroma, T565lpxr) and filtered by emission filters in both separated emission light paths (Semrock, 525/50 nm Brightline single-band band-pass filter, FF03-525/50-25; and Semrock, 630/92 nm Brightline single-band band-pass filter, FF01-630/92-25) inside a two-way image splitter (Cairn Research, Optosplit II), and for dual-colour imaging imaged side by side on an EMCCD camera (Andor, iXon 897, DU-897E-COO-#BV). For single-colour imaging the other emission light path was blocked. Additional 1.5× (inside Eclipse Ti) and 2× (inside Optosplit II) intermediate magnification resulted in one camera pixel corresponding to 92 nm × 92 nm in the image plane.

For some of the experiments an almost identical microscope was used. This microscope differed in objective (Nikon, CFI Apo TIRF 100×, N.A.: 1.49) and employed a Cairn Research Optosplit III. In this instrument, the following filters were used; a dichroic mirror in the excitation path (Semrock, 405/488/561/635 nm lasers Brightline quad-edge laser-flat, Di01-R405/488/561/635-25×36). Emission light was separated inside the Optosplit III using a dichroic long-pass filter (Semrock, 580 nm edge Brightline single-edge imaging flat, FF580-FDi01-25×36) and filtered by emission filters in both separated emission light paths (Semrock, 525/45 nm Brightline single-band band-pass filter, FF01-525/45-25; and Semrock, 609/54 nm Brightline single-band band-pass filter, FF01-609/54-25). Additional 2× (inside Optosplit III) intermediate magnification resulted in one camera pixel corresponding to 80 nm × 80 nm in the image plane.

***C. elegans* strains.** The *C. elegans* strains used in this study are listed in Supplementary Table 1. Strains carrying integrated single-copy transgenes encoding for fluorescently labelled IFT components were constructed using the MosSCI method as previously described[59]. Integration of transgenes was confirmed by PCR of regions spanning each side of the insertion. Worm maintenance and genetic crosses were performed using standard *C. elegans* techniques[60].

***C. elegans* imaging.** Fluorescence imaging in living *C. elegans* hermaphrodite worms was performed using modifications of ref. 61 by anaesthetizing adult worms (maintained at 20 °C) in M9 containing 5 mM levamisole (Sigma, tetramisole hydrochloride, L9756), and immobilizing them between a 2% agarose (Roche, Agarose MP, 11 388 991 001) in M9 pad and a 22 × 22 mm cover glass (Marienfeld, High Precision No. 1.5H, 0107052), sealed with VaLaP (equal parts of vaseline, lanolin and paraffin wax) to prevent media evaporation. Samples were imaged at room temperature (21 °C), in most experiments, at 152 ms per frame at 5.3× pre-amplifier gain and 300 EM gain with 10 MHz ADC readout. Typically, for each phasmid cilium 150 frames were recorded. For further data processing images were only taken into account when the nematode was oriented in such a way that most of the cilium (always including the base) was in focus. Number of worms and number of phasmid cilia measured are noted in Supplementary Fig. 6 for each strain. Cilia were measured only once (obtaining one kymograph per phasmid cilium), except for OSM-6::eGFP strains EJP76 and EJP77, for which additional image series could be taken because of low photobleaching due to high signal levels.

Kymograph generation and analysis. Images were analysed by generating kymographs using a custom-written ImageJ (http://imagej.nih.gov/ij) plugin. Fourier filtering allowed for separation of the three different motility components (that is, forward, backward and static) into three separate kymographs. These kymographs were analysed using custom-written routines in LabVIEW (National Instruments), based on peak detection and cross-correlation. The kymograph generation and analysis software can be downloaded at: http://www.nat.vu.nl/~erwinp/downloads.html.

Single-molecule analysis. Images were analysed using custom-written routines in MATLAB (MathWorks). For each image, intensity profiles of individual fluorophores were fitted with a two-dimensional Gaussian to obtain their location and intensity. Subsequently, the localizations in subsequent image frames were linked to obtain single-molecule trajectories using a linking algorithm[62]. Super-resolution images (SRI) were generated by accumulating individual localizations of multiple single-molecule trajectories (each localization is rendered with a two-dimensional Gaussian of width 40 nm (s.d.), the approximate localization precision). The SRIs allowed accurate determination of the four ciliary subdomains: base, transition zone, proximal segment and distal segment. A spline was drawn on top of the SRI to define a local two-dimensional coordinate system (x axis parallel and y axis perpendicular to ciliary long axis). For further data processing, all single-molecule localizations were transformed to this ciliary coordinate system.

Turnaround events were identified in trajectories that exhibited a local minimum or maximum in the x-coordinate. To suppress noise-induced false positives, turnarounds were scored only when this extremum was preceded and followed by at least three consecutive steps in the same direction with an average displacement of at least 46 nm in each direction (twice the expected standard error of the mean of three displacements in each direction due to the localization accuracy, assumed 40 nm). Turnaround locations (extrema) from the selected trajectories were determined with respect to the ciliary base using SRIs (see above). Pauses at turnarounds were identified in trajectories at localizations where the preceding and subsequent displacements were on average less than 28 nm (the standard error of the mean of the two displacements due to the localization accuracy).

Trajectories in the anterograde direction were assigned to the ciliary subdomains on the basis of the position of the first time point. Escape times were defined as the minimum time a tracked molecule (motor, IFT-particle subcomplex) required to move at least 100 nm away from its starting point. Trajectories that did not cover this 100 nm distance, for example, owing to photobleaching, were not considered.

Quantification of fluorescence intensities. Single eGFP intensities were measured *in vitro* using *Escherichia coli* expressed and purified fluorescent proteins in imaging buffer (50 mM Tris, pH 8.0, 100 mM NaCl, 2 mM $MgCl_2$) immobilized on a 22 × 22 mm cover glass (Marienfeld, High Precision No. 1.5H, 0107052). Identical intensities (within experimental uncertainty) were obtained *in vivo*, using the EJP13 strains (Supplementary Table 1).

To be able to quantitatively compare eGFP and mCherry intensities, we measured the cilium-averaged integrated fluorescence intensity of the KAP-1::eGFP (EJP13) and KAP-1::mCherry (EJP85) strains and compared them at different excitation powers (Supplementary Fig. 6l). From the relative slopes of the fluorescence intensity versus excitation power a correction factor was obtained to convert measured mCherry intensity into eGFP intensity expected under the same conditions (instrument, excitation intensity). Under our imaging conditions, photobleaching of mCherry was far more severe than eGFP, which precluded quantitative comparison of fluorescence intensities in two-colour experiments on double-labelled strains (EJP42, kymographs in Fig. 2c,f). Therefore, quantification of the number of motors was performed on strains expressing only one kind of the fluorescently tagged motors (EJP13 and EJP16, train intensity traces in Fig. 2c,f).

Fluorescence quantifications are presented throughout this paper in three different ways. The first is by means of profiles of individual cilia, which are presented normalized to their maximum. We note that the shape of the phasmid cilia is such that the whole cilium cannot be captured in a single image plane. In most of the cilia presented here, the tip extremity (last ∼1 μm) was not in focus and therefore not analysed. The second representation is by average cilium-intensity profiles, obtained by averaging the profiles of multiple individual cilia. These averaged intensities are corrected for imaging conditions and probe used, such that they can be compared quantitatively throughout the paper. The third representation is by train intensities obtained from kymographs, which are converted to number of proteins by first correcting for imaging conditions and probe and second dividing their intensity by that of the average intensity of a single eGFP molecule.

Modelling of the motor-fraction train-velocity relation. Alternating action model[10]:

$$v_{\text{IFT-train}} = \frac{v_{\text{kinesin-II}}\, v_{\text{osm-3}}}{\alpha v_{\text{kinesin-II}} + (1-\alpha) v_{\text{osm-3}}}$$

with α being the motor fraction of OSM-3 (ref. 10):

$$\alpha = \frac{N_{\text{osm-3}}}{N_{\text{osm-3}} + M_{\text{kinesin-II}}}$$

In our biased contribution model an additional parameter γ is added to the motor fraction relation:

$$\alpha' = \frac{\gamma N_{\text{osm-3}}}{\gamma N_{\text{osm-3}} + M_{\text{kinesin-II}}}$$

The new α' is used in place of α in the alternating action model resulting in the biased contribution model:

$$v_{\text{IFT-train}} = \frac{v_{\text{kinesin-II}} v_{\text{osm-3}} [\alpha\gamma + (1-\alpha)]}{\alpha\gamma v_{\text{kinesin-II}} + (1-\alpha) v_{\text{osm-3}}}$$

Note, the biased contribution model is mathematically identical to the mechanical competition model with γ being the stall-force ratio[10]:

$$\gamma = \frac{F^{\text{stall}}_{\text{osm-3}}}{F^{\text{stall}}_{\text{kinesin-II}}}$$

Simulations of single-motor dynamics underlying ciliary distribution. Stochastic simulations were performed using custom-written routines in LabVIEW (National Instruments). Single motors moved repetitively along a 9,000 nm track with 1 nm steps. Motors moved in anterograde or retrograde directions with position-dependent velocities equal to those measured for the IFT-B-particle subcomplexes (Fig. 2b and Supplementary Fig. 2c). Motors turned around stochastically in A-to-R and R-to-A directions. Turnaround probabilities were determined using either constant probability per time interval or position-dependent probability distributions. Motors started moving at the zero position in the anterograde direction and underwent 10,000 turnaround events. From such trajectories, histograms of turnaround locations were determined as well as time-averaged intensity profiles. Histograms and intensity profiles were multiplied by $2-(1/(e^{(x-4{,}500)/200}+1))$ to account for the overlap of the two phasmid cilia in the DS region (Fig. 1a). Intensity profiles were convoluted with a Gaussian function to account for the resolution of our instrument (approximately 300 nm). Input parameters of the simulations were optimized to obtain qualitative similarity with experimental results. For kinesin-II an intensity profile was used peaking at B and TZ and decaying within several micrometres in the PS and turnarounds occurring in the same region. For OSM-3 a broad intensity profile was used with increased intensity throughout DS and A-to-R turnarounds occurring increasingly towards the tip and R-to-A turnarounds increasingly towards the base. The simulation software can be downloaded at: http://www.nat.vu.nl/~erwinp/downloads.html.

59. Frokjaer-Jensen, C. *et al.* Single-copy insertion of transgenes in *Caenorhabditis elegans*. *Nat. Genet.* **40,** 1375–1383 (2008).
60. Brenner, S. Genetics of *Caenorhabditis elegans*. *Genetics* **77,** 71–94 (1974).
61. Brust-Mascher, I., Ou, G. S. & Scholey, J. M. Measuring rates of intraflagellar transport along *Caenorhabditis elegans* sensory cilia using fluorescence microscopy. *Method Enzymol.* **524,** 285–304 (2013).
62. Jaqaman, K. *et al.* Robust single-particle tracking in live-cell time-lapse sequences. *Nat. Methods* **5,** 695–702 (2008).

DOI: 10.1038/ncb3263

nature cell biology

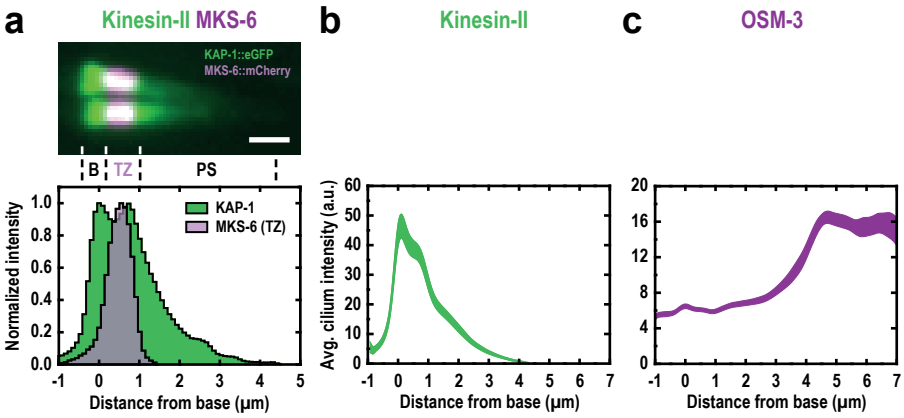

Supplementary Figure 1 IFT-particle subcomplexes and IFT-motors show distinct localization patterns along cilia (related to Fig. 1). (**a**) Representative two-color time-averaged fluorescence image of kinesin-II (green) and transition zone marker MKS-6 (magenta) (*top*), and corresponding fluorescence-intensity profile (*bottom*) along the lower cilium (same data as inset Fig. *1d*) from 20 worms. Scale bar, 1 μm. (**b,c**) Average fluorescence-intensity profiles obtained from time-averaged fluorescence images (22.5 s each) of multiple different phasmid cilia. Line thickness represents 95% confidence interval of the mean (CIM). (**b**) Kinesin-II pooled from 15 worms, 30 phasmid cilia. (**c**) OSM-3 pooled from 19 worms, 32 phasmid cilia. (**a**-**c**) B – Base, TZ – Transition Zone, PS – Proximal Segment and DS – Distal Segment.

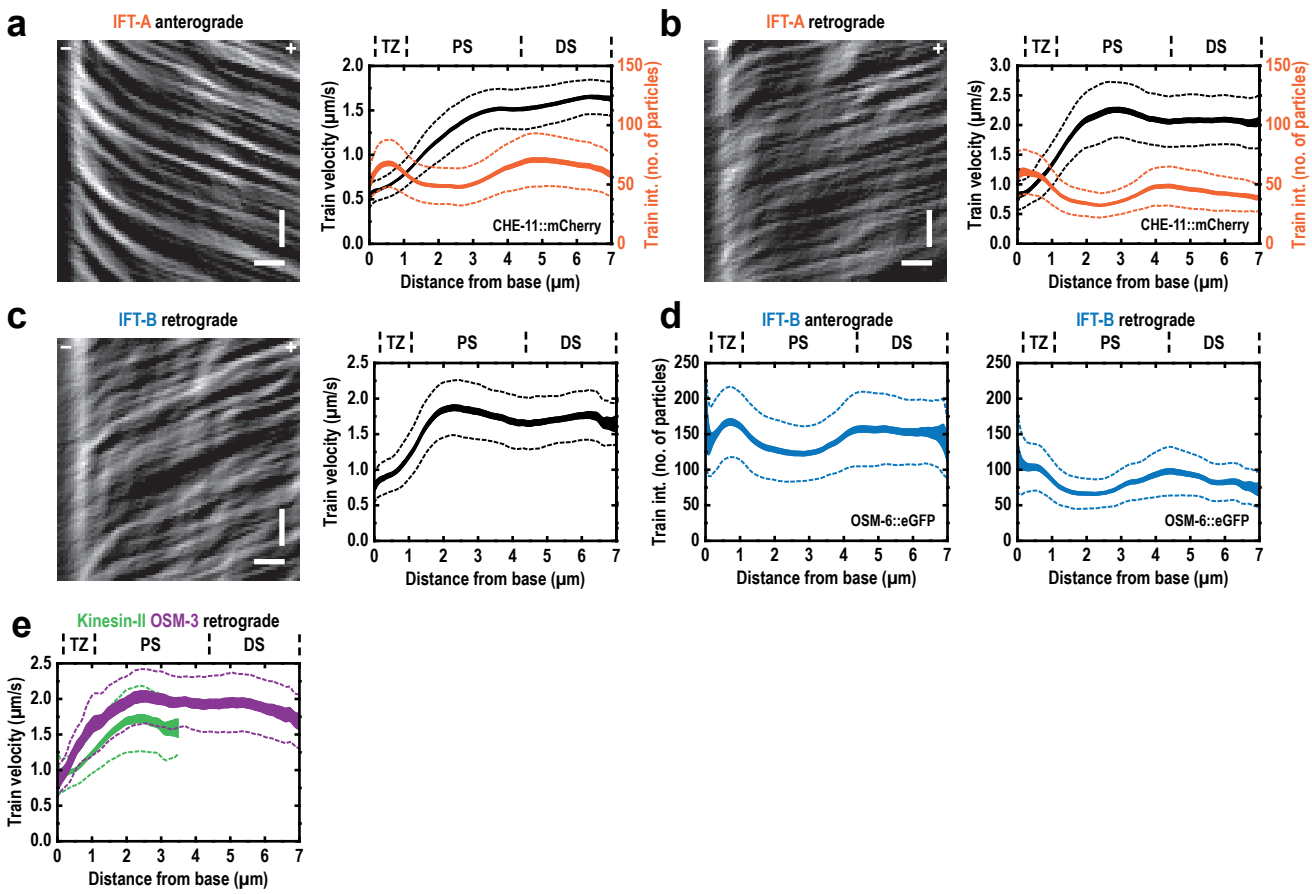

Supplementary Figure 2 Kinesin-2 motors cooperate to transport IFT-trains along cilia (related to Fig. 2). (**a**,**b**) Representative anterograde (**a**) and retrograde (**b**) Fourier-filtered kymographs of IFT-A particle subcomplexes and corresponding train velocity (black) and train intensity (orange). (**c**) Representative retrograde Fourier-filtered kymograph of IFT-B particle subcomplexes and corresponding train velocity. (**d**) Average IFT-B intensity for (*left*) anterograde and (*right*) retrograde trains. (**e**) Velocities of retrograde transport of kinesin-II (green) and OSM-3 (magenta). (**a**-**e**) Minus (-) and plus (+) denote MT-polarity, horizontal scale bars, 1 µm; vertical scale bars, 2 s. Dashed lines represent mean ± SD, line thickness represents 95% CIM. For number of kymograph trajectories included and number of worms imaged to obtain representative images see Supplementary Fig. 6a-d.

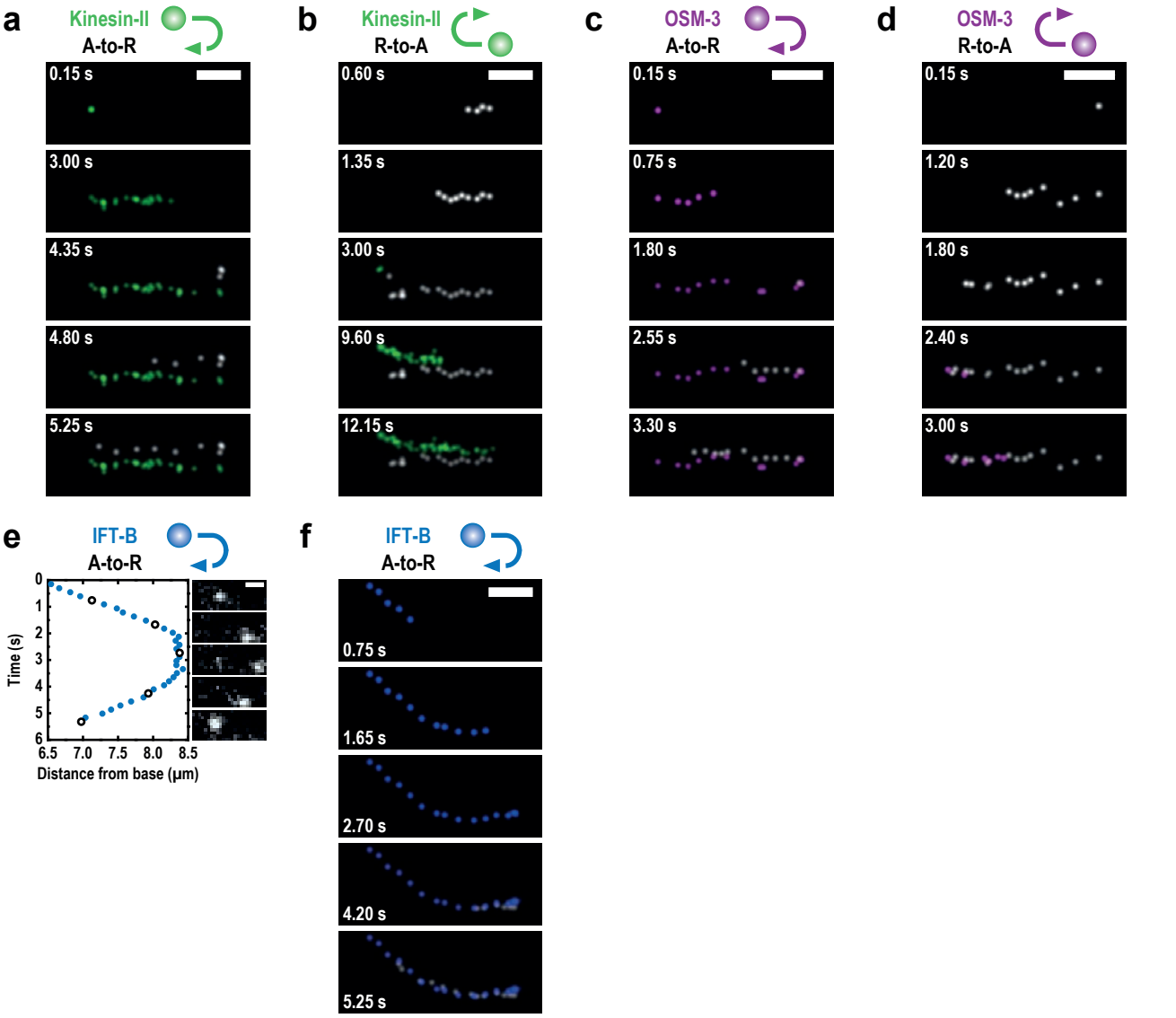

Supplementary Figure 3 Single-motor turnarounds result in confinement of kinesin-II close to the base and OSM-3 near the distal segment (related to Fig. 3). (**a**) All localizations of the kinesin-II anterograde-to-retrograde (A-to-R) trajectory of Figure *3b* in main text; a single kinesin-II motor initially moves in the anterograde direction (green), suddenly switches direction, to move in retrograde direction (grey), being transported by IFT-dynein. (**b**) All localizations of the kinesin-II retrograde-to-anterograde (R-to-A) trajectory of Figure *3d* in main text; a single kinesin-II motor first moves in the retrograde direction (grey), transported by IFT-dynein, waits at the base, and next moves in the opposite, anterograde direction (green). (**c**) All localizations of the OSM-3 A-to-R trajectory of Figure *3f* in main text; a single OSM-3 motor initially moves in the anterograde direction (magenta), suddenly switches direction into the retrograde direction (grey), transported by IFT-dynein. (**d**) All localizations of the OSM-3 R-to-A trajectory of Figure *3h* in main text; a single OSM-3 motor initially moves in the retrograde direction (grey), carried by IFT-dynein, and suddenly switches direction just before the base, moving in the anterograde direction (magenta). (**e**) One representative single-particle trajectory (*left*) and corresponding images (*right*, indicated by open symbols in trajectories) of an IFT-B particle subcomplex A-to-R turnaround from 10 worms, 20 phasmid cilia. (**f**) All localizations of the IFT-B A-to-R trajectory of Supplementary Figure *3e*; Scale bars, 0.5 µm.

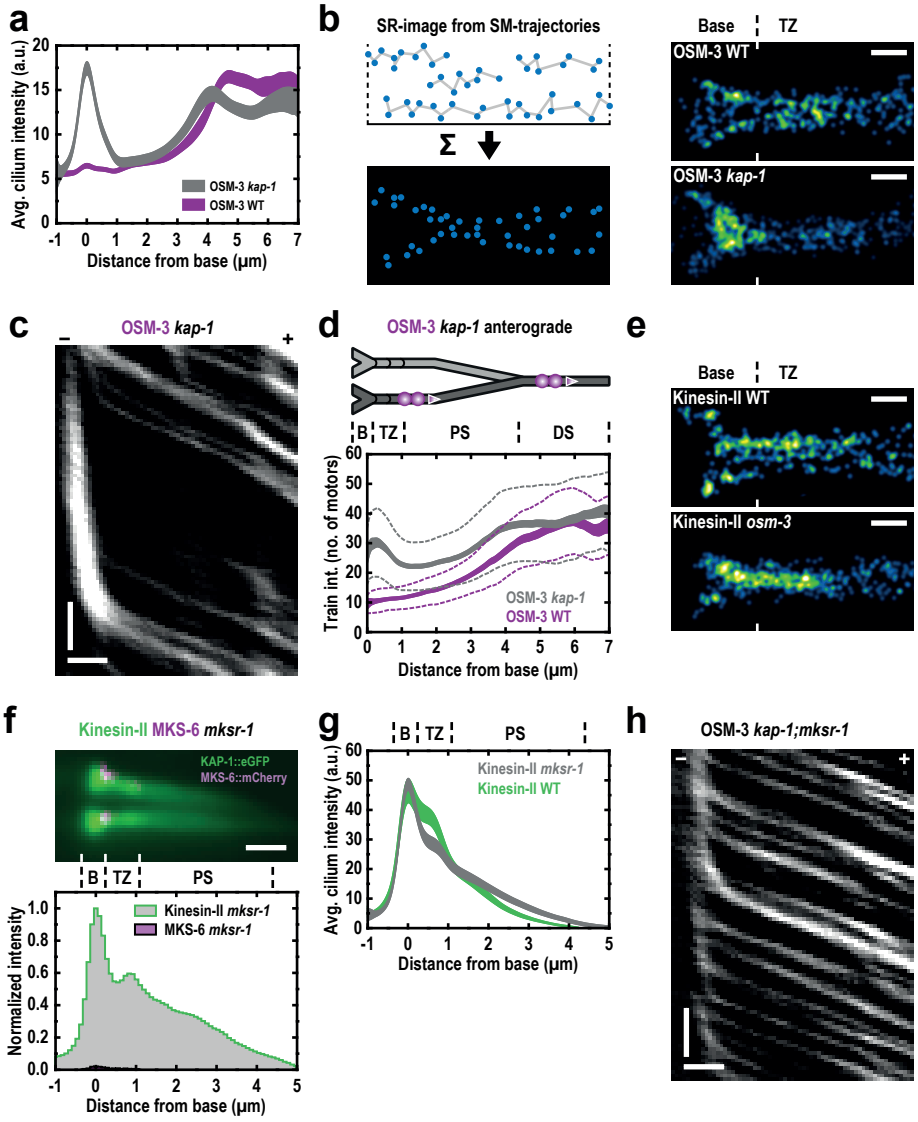

Supplementary Figure 4 Mutants with IFT-motor defects and transition-zone defects reveal that kinesin-II navigates IFT-trains into the proximal segment, where OSM-3 takes over and drives fast, long-distance transport (related to Fig. 5). (**a**) Fluorescence-intensity profiles obtained from time-averaged fluorescence images (22.5 s each) of multiple different phasmid cilia. Comparison of OSM-3 in kinesin-II mutant background (*kap-1*; grey, pooled 25 worms, 46 phasmid cilia) and wild-type OSM-3 (magenta, pooled from 19 worms, 32 phasmid cilia, from Supplementary Figure *1c*) reveals a ~three-fold difference in OSM-3 intensity at the base. (**b**) Representative super-resolution (SR) images obtained by accumulating (Σ) localizations (blue dots) of multiple single-molecule trajectories (grey lines) for OSM-3 (*top right*; from 20 worms, 31 phasmid cilia) and OSM-3 in a kinesin-II mutant background (*kap-1*; *bottom right*; from 11 worms, 18 phasmid cilia), see also Supplementary Figure *6i*. (**c**) Representative anterograde Fourier-filtered kymograph of OSM-3 in a kinesin-II mutant background (*kap-1*). (**d**) Average OSM-3 intensity for anterograde trains in *C. elegans* strains lacking (*kap-1*; grey) and containing (magenta) functional kinesin-II. (**e**) Representative super-resolution images for kinesin-II (*top right*; from 12 worms, 15 phasmid cilia) and kinesinII in an OSM-3 mutant background (*osm-3*; *bottom right*; from 20 worms, 34 phasmid cilia, see also Supplementary Figure *6j*. (**f**) Representative (from 20 worms) two-color time-averaged fluorescence image of kinesin-II (green) and transition zone marker MKS-6 (magenta) (*top*), and corresponding fluorescence-intensity profile (*bottom*) along the lower cilium. Scale bar, 1 µm. The fluorescence-intensity profile of kinesin-II is normalized to its maximum and that of MKS-6 is scaled relative to MKS-6 in wild type (Supplementary Figure *1a*). (**g**) Average fluorescence-intensity profiles obtained from time-averaged fluorescence images (22.5 s each) of multiple phasmid cilia. Comparison of kinesin-II in MKSR-1 mutant background (*mksr-1*; grey, pooled from 22 worms, 42 phasmid cilia) and wild-type kinesin-II (green, pooled from 15 worms, 30 phasmid cilia, from Supplementary Figure *1b*) reveals a decrease of kinesin-II in the TZ but an increase in the PS. (**h**) Representative anterograde Fourier-filtered kymograph of OSM-3 in a kinesin-II and MKSR-1 double-mutant background (*kap-1;mksr-1*). (**b,e**) Scale bars, 0.25 µm. (**c,h**) Minus (-) and plus (+) denote MT-polarity, horizontal scale bar, 1 µm; vertical scale bar, 2 s. (**a,d,g**) Dashed lines are means ± SD, line thickness represents 95% CIM. For number of kymograph trajectories included and number of worms imaged to obtain representative kymographs see Supplementary Fig. 6d-g,i,j.

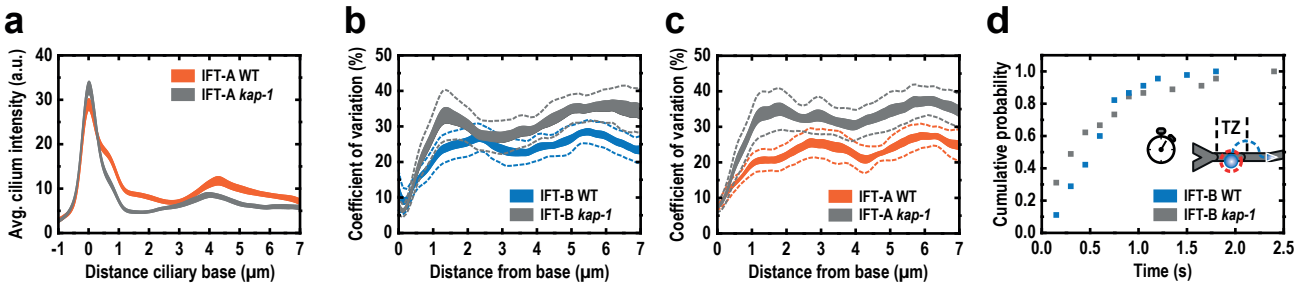

Supplementary Figure 5 IFT-particle subcomplex loading and distribution is altered in the absence of kinesin-II (related to Fig. 6). (**a**) Average fluorescence-intensity profiles obtained from time-averaged fluorescence images (22.5 s each) of multiple different phasmid cilia. IFT-A in kinesin-II mutant background (*kap-1*; grey, pooled from 22 worms, 44 phasmid cilia), and wild-type IFT-A (orange, pooled from 25 worms, 50 phasmid cilia). (**b**) Coefficient of variation (standard deviation divided by the mean) of kymographs obtained from image stacks of IFT-B in *C. elegans* strains lacking (*kap-1*; grey, $n = 40$ kymographs from 17 worms, 40 phasmid cilia) and containing (blue, $n = 52$ kymographs from 19 worms, 52 phasmid cilia) functional kinesin-II show that kymographs of *C. elegans* strains lacking kinesin-II are less regular. (**c**) Coefficient of variation (standard deviation divided by the mean) of kymographs obtained from image stacks of IFT-A in *C. elegans* strains lacking (*kap-1*; grey, $n = 36$ kymographs from 22 worms, 36 phasmid cilia) and containing (orange, $n = 50$ kymographs from 25 worms, 50 phasmid cilia) functional kinesin-II show that kymographs of *C. elegans* strains lacking kinesin-II are less regular. (**d**) Cumulative probability distribution of the durations of single particle subcomplexes escaping from the transition zone. Distributions are obtained by defining a region of interest and measuring the time it takes for a particle subcomplex to cross the boundary in anterograde direction (*inset*). IFT-B particle subcomplexes escaped the transition zone in 0.6 ± 0.1 s (mean ± s.e.m., $n = 45$ IFT-B particle subcomplexes from 10 worms, 19 phasmid cilia) in the presence of kinesin-II and in 0.6 ± 0.1 s (mean ± s.e.m., $n = 45$ IFT-B particle subcomplexes from 25 worms, 38 phasmid cilia) lacking functional kinesin-II (*kap-1*). Dashed lines are mean ± SD, line thickness represents 95% CIM.

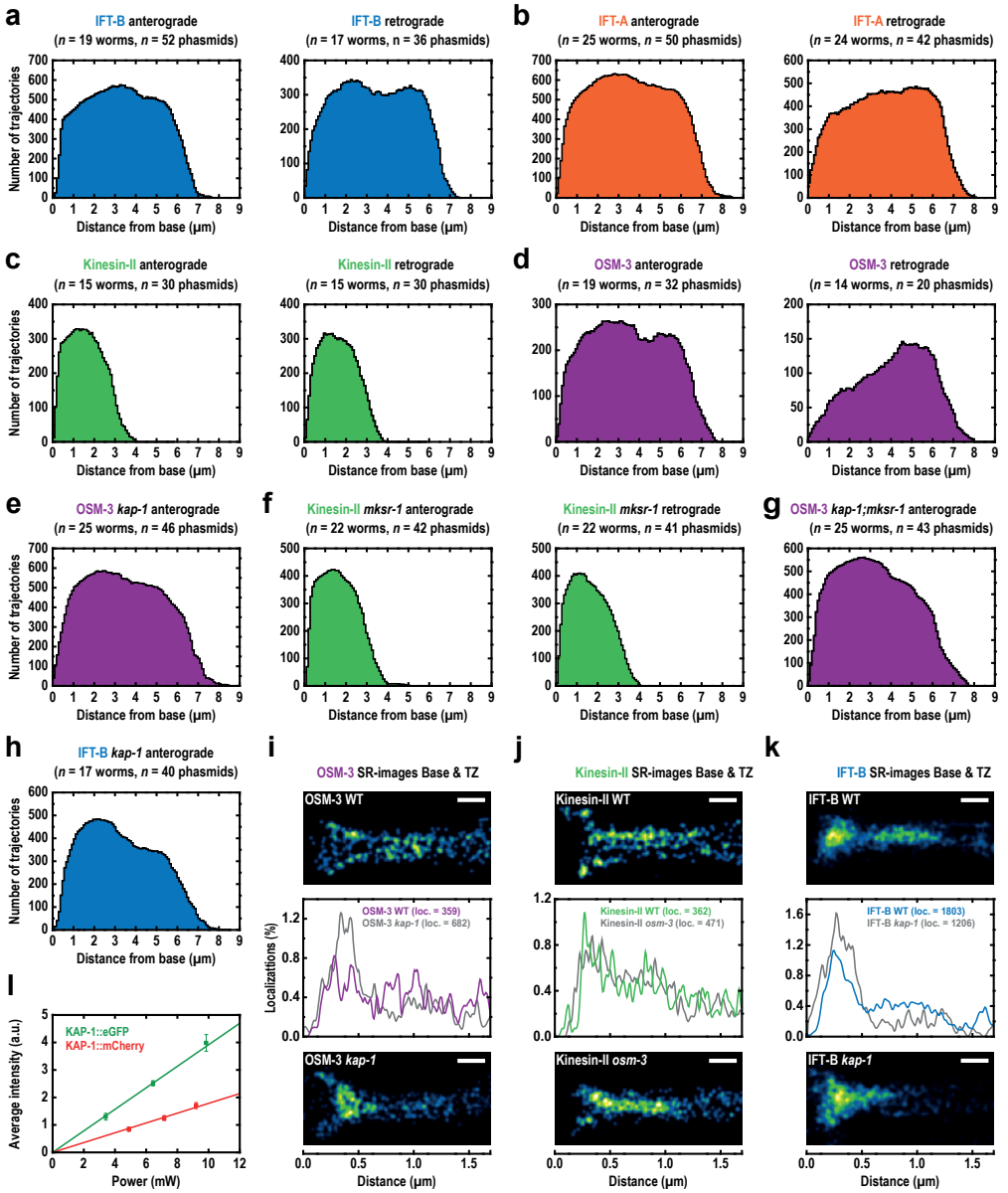

Supplementary Figure 6 Histograms of the amount of kymograph trajectories used to analyze train dynamics and intensities, the distribution and number of localizations used to build the super-resolution (SR) images, and *in vivo* comparison of eGFP and mCherry intensity (related to multiple figures and experimental procedures (see legend)). (**a**) IFT-B, (*left*) anterograde trains (corresponding to *Figure 1c; Table 1; Figure 2b,d,e; Supplementary Figure 2d*; *Figure 6b,d*) and (*right*) retrograde trains (corresponding to *Supplementary figure 2c,d*). (**b**) IFT-A, (*left*) anterograde trains (corresponding to *Figure 1b; Table 1; Supplementary Figure 2a*) and (*right*) retrograde trains (corresponding to *Supplementary Figure 2b*). (**c**) Kinesin-II, (*left*) anterograde trains (corresponding to *Figure 1d; Table 1; Figure 2c,d,e*; *Figure 5h (top),i*) and (*right*) retrograde trains (corresponding to *Figure 2f*; *Supplementary Figure 2e; Figure 5j*). (**d**) OSM-3, (*left*) anterograde trains (corresponding to *Figure 1e; Table 1; Figure 2c,d,e; Figure 5c*; *Supplementary Figure 4d*) and (*right*) retrograde trains (corresponding to *Figure 2f*; *Supplementary Figure 2e*). (**e**) Anterograde OSM-3 in a kinesin-II mutant background (*kap-1*; corresponding to *Table 1; Figure 5a-c,k; Supplementary Figure 4c,d*). (**f**) Anterograde (*left*) (corresponding to *Table 1; Figure 5h (bottom),i*) and retrograde (*right*) (corresponding to *Figure 5j*) kinesin-II in an MKSR-1 mutant background (*mksr-1*). (**g**) Anterograde OSM-3 in a kinesin-II and MKSR-1 double-mutant background (*kap-1;mksr-1*; corresponding to *Figure 5k; Supplementary Figure 4h*). (**h**) Anterograde IFT-B in a kinesin-II mutant background (*kap-1*; corresponding to *Table 1; Figure 6c,d*). (**i-k**) SR-images (*top* and *bottom*) and projection of localizations along long image axis (*middle*, area for each trace normalized), Related to Figure 6 and Supplementary Figure 4. (**i**) OSM-3, from *Supplementary Figure 4b*; (**j**) Kinesin-II, from *Supplementary Figure 4e*; (**k**) IFT-B, from *Figure 6e*. Scale bar: 0.25 µm. (**l**) Fluorescence intensities of eGFP-tagged (EJP13) and mCherry-tagged (EJP85) KAP-1 as a function of excitation intensity. Intensities were obtained by integrating a cilium region of interest (~1.7 µm^2) over the first ten frames of an image series and averaging over 12 to 20 phasmid cilia (6 to 14 worms for each data point) for each imaging condition. Error bars represents s.e.m.. Linear fits are used to calculate a mCherry to eGFP fluorescence intensity correction factor of 2.2, Related to "Quantification of fluorescence intensities" in Methods.

Strain	Genotype	Short notation
EJP13	*kap-1(ok676) III; vuaSi1 [pBP20; Pkap-1::kap-1::eGFP; cb-unc-119(+)] IV*	Kinesin-II or Kinesin-II WT
EJP16	*vuaSi2 [pBP22; Posm-3::osm-3::mCherry; cb-unc-119(+)] II; unc-119(ed3) III; osm-3(p802) IV*	OSM-3 or OSM-3 WT
EJP18	*vuaSi2 [pBP22; Posm-3::osm-3::mCherry; cb-unc-119(+)] II; kap-1(ok676) III; vuaSi4 [pBP30; Pkap-1::kap-1::paGFP; cb-unc-119(+)] IV*	
EJP22	*vuaSi2 [pBP22; Posm-3::osm-3::mCherry; cb-unc-119(+)] II; kap-1(ok676) III; osm-3(p802) IV*	OSM-3 *kap-1*
EJP34	*vuaSi8 [pBP31; Posm-3::osm-3::paGFP; cb-unc-119(+)] II; kap-1(ok676) III; vuaSi9 [pBP27; Pkap-1::kap-1::mCherry; cb-unc-119(+)] IV*	
EJP41	*vuaSi10 [pBP33; Pkap-1::kap-1::eGFP; cb-unc-119(+)] I; kap-1(ok676) III; osm-3(p802) IV*	Kinesin-II *osm-3*
EJP42	*vuaSi10 [pBP33; Pkap-1::kap-1::eGFP; cb-unc-119(+)] I; vuaSi2 [pBP22; Posm-3::osm-3::mCherry; cb-unc-119(+)] II; kap-1(ok676) III; osm-3(p802) IV*	Kinesin-II OSM-3
EJP64	*kap-1(ok676) III; vuaSi1 [pBP20; Pkap-1::kap-1::eGFP; cb-unc-119(+)] IV; mksr-1(ok2092) X*	Kinesin-II *mksr-1*
EJP70	*mks-6(gk674) I; vuaSi21 [pBP39; Pmks-6::mks-6::mCherry; cb-unc-119(+)] II; kap-1(ok676) III; vuaSi1 [pBP20; Pkap-1::kap-1::eGFP; cb-unc-119(+)] IV*	Kinesin-II MKS-6
EJP71	*mks-6(gk674) I; vuaSi21 [pBP39; Pmks-6::mks-6::mCherry; cb-unc-119(+)] II; kap-1(ok676) III; vuaSi1 [pBP20; Pkap-1::kap-1::eGFP; cb-unc-119(+)] IV; mksr-1(ok2092) X*	Kinesin-II MKS-6 *mksr-1*
EJP73	*vuaSi2 [pBP22; Posm-3::osm-3::mCherry; cb-unc-119(+)] II; kap-1(ok676) III; osm-3(p802) IV; mksr-1(ok2092) X*	OSM-3 *kap-1;mksr-1*
EJP76	*vuaSi15 [pBP36; Posm-6::osm-6::eGFP; cb-unc-119(+)] I; unc-119(ed3) III; osm-6(p811) V*	IFT-B or IFT-B WT
EJP77	*vuaSi15 [pBP36; Posm-6::osm-6::eGFP; cb-unc-119(+)] I; kap-1(ok676) III; osm-6(p811) V*	IFT-B *kap-1*
EJP81	*vuaSi24 [pBP43; Pche-11::che-11::mCherry; cb-unc-119(+)] II; unc-119(ed3) III; che-11(tm3433) V*	IFT-A or IFT-A WT
EJP82	*vuaSi24 [pBP43; Pche-11::che-11::mCherry; cb-unc-119(+)] II; kap-1(ok676) III; che-11(tm3433) V*	IFT-A *kap-1*
EJP85	*kap-1(ok676) III; vuaSi9 [pBP27; Pkap-1::kap-1::mCherry; cb-unc-119(+)] IV*	

Supplementary Table . *C. elegans* strains used in this study. Short notation is used throughout main text and figures to increase readability.

Supplementary Video Legends

Supplementary Video 1 Dynamics of IFT-B in *C. elegans* strain EJP76. Video plays at twice real time (time indicated). Scale bar, 2 µm. Related to Figure 1c; Figure 2b; Supplementary Figure 2c.

Supplementary Video 2 Dynamics of kinesin-II (green) and OSM-3 (magenta) in *C. elegans* strain EJP42. Video plays at twice real time (time indicated). Scale bar, 2 µm. Related to Figure 2c,f.

Supplementary Video 3 Single-molecule dynamics of kinesin-II in *C. elegans* strain EJP13. Video plays at twice real time (time indicated). Scale bar, 1 µm. Related to Figure 3b,d.

Supplementary Video 4 All single-molecule localizations of Supplementary Video 3 of kinesin-II in *C. elegans* strain EJP13. Video plays at twice real time (time indicated). Scale bar, 1 µm. Related to Figure 3b,d.

Supplementary Video 5 Dynamics of OSM-3 in the absence of functional kinesin-II in *C. elegans* strain EJP22. Video plays at twice real time (time indicated). Scale bar, 2 µm. Related to Figure 5a-c.

Supplementary Video 6 Dynamics of kinesin-II in the absence of OSM-3 in *C. elegans* strain EJP41. Video plays at twice real time (time indicated). Scale bar, 2 µm. Related to Figure 5d,e.

Supplementary Video 7 Dynamics of kinesin-II in transition-zone mutant *C. elegans* strain EJP64. Video plays at twice real time (time indicated). Scale bar, 2 µm. Related to Figure 5g-j.